ANALOG AND NUMERICAL EXPERIMENTS INVESTIGATING FORCE CHAIN INFLUENCES ON THE BED PHYSICS OF DENSE GRANULAR FLOWS

A Dissertation
Presented to
The Academic Faculty

by

Joseph Jeremiah Estep

In Partial Fulfillment
of the Requirements for the Degree
Doctor of Philosophy in the
School of Earth and Atmospheric Sciences, Georgia Institute of Technology

Georgia Institute of Technology
May 2014

ANALOG AND NUMERICAL EXPERIMENTS INVESTIGATING FORCE CHAIN INFLUENCES ON THE BED PHYSICS OF DENSE GRANULAR FLOWS

Approved by:

Dr. Josef Dufek, Advisor
School of Earth and Atmospheric Sciences
Georgia Institute of Technology

Dr. Chris Huber
School of Earth and Atmospheric Sciences
Georgia Institute of Technology

Dr. Andy Newman
School of Earth and Atmospheric Sciences
Georgia Institute of Technology

Dr. Hermann Fritz
School of Civil and Environmental Engineering
Georgia Institute of Technology

Dr. Zhigang Peng
School of Earth and Atmospheric Sciences
Georgia Institute of Technology

Date Approved: March 12, 2014

To James Harold Hitchcock III, 6/27/1982 – 2/5/2014

ACKNOWLEDGEMENTS

I wish to thank my parents, Bob and Sandra Estep, for infinite love, unwavering support, and continued inspiration during my journey that has lead to this hallmark achievement. To my wife, Jamie, and all the family and friends that have encouraged me towards this end I bestow my most sincere gratitude. To my advisor, Dr. Josef Dufek, I owe a great multitude of thanks pertaining to guidance for academic, research, and life related puzzles, as well as the opportunity to work with him. I greatly appreciate the efforts of my faculty committee who have graciously agreed to review this work on my behalf, and often have provided me with useful and insightful consultation. I am honored not only to have the favorable circumstance to share ideas with and learn from my advisor and committee, but also for the good fortune to know them as friends. I also wish thank the Georgia Institute of Technology for allowing me the opportunity to pursue my education in a preeminent university, which just so happens to have been my favorite since childhood.

What's the good word? To hell with Georgia! How 'bout them dogs? Piss on 'em!

TABLE OF CONTENTS

LIST OF TABLES

LIST OF FIGURES

SUMMARY

Granular materials are composed of solid, discrete particles and exhibit mechanical properties that range from fluid to solid behavior. Some of the complexity exhibited by granular systems arises due to the long-range order that develops due to particle-particle contact. Inter-particle forces in granular materials often form a distributive network of filamentary force-accommodating chains (i.e. force chains), such that a fraction of the total number of particles accommodates the majority of the forces in the system. The force chain network inherent to a system composed of granular materials controls the macroscopic behavior of the granular material. Force transmission by these filamentary chains is focused (or localized) to the grain scale at boundaries such as the granular flow substrate. Recent laboratory experiments have shown that force chains transmit extreme localized forces to the substrates of free surface granular flows. In this work we combine analog and numeric experimental approaches to investigate the forces at the bed of a simplified granular flow. A photoelastic experimental approach is used to resolve discrete forces in the granular flows. We also conduct discrete element method (DEM) simulations, using input parameters derived from measureable physical material properties of experimental and natural materials, which successfully reproduce the analog experimental results. This work suggests that force chain activity may play an unexpected and important role in the bed physics of dense granular flows through substrate modification by erosion and entrainment, and that DEM

numerical methods effectively treat force chain processes in simulated granular flows.

CHAPTER 1. INTRODUCTION

Granular materials are composed of solid, discrete particles that dissipate energy when the constitutive particles interact – for example, through friction or collision [*Behringer et al.*, 2008]. Granular materials exhibit mechanical properties that range from fluid to solid behavior and granular materials can have varied rheological response when in an excited state, that is when the materials are vibrated or allowed to flow [*Frey and Church*, 2011; *Jaeger et al.,* 1996; *Sun et al.,* 2010]. Rheology of granular materials is principal to a suite of geophysical processes, including dry ravel, sand dune migration, the motion of landslides, debris flows, pyroclastic flows, block and ash flows, avalanches, and fault systems [*Daniels and Hayman*, 2008; *Dufek and Bergantz*, 2007; *Furbish et al.*, 2008; *Iverson et al.,* 2011; *LaBerge et al.*, 2006; *Majmudar et al.*, 2005].

Recent experimental studies have highlighted that inter-particle forces in granular materials often form a distributive network of filamentary force-accommodating chains (i.e. force chains) as opposed to having an isotropic distribution of forces, such that a fraction of the total number of particles accommodate the majority of body forces and externally applied forces [*Geng et al.,* 2003; *Majmudar and Behringer*, 2005; *Behringer et al.;* 2008; *Sun et al.*, 2010]. Figure 1 illustrates an idealized force chain network in a granular flow down an incline, where the force chain participants are indicated by shaded particles.

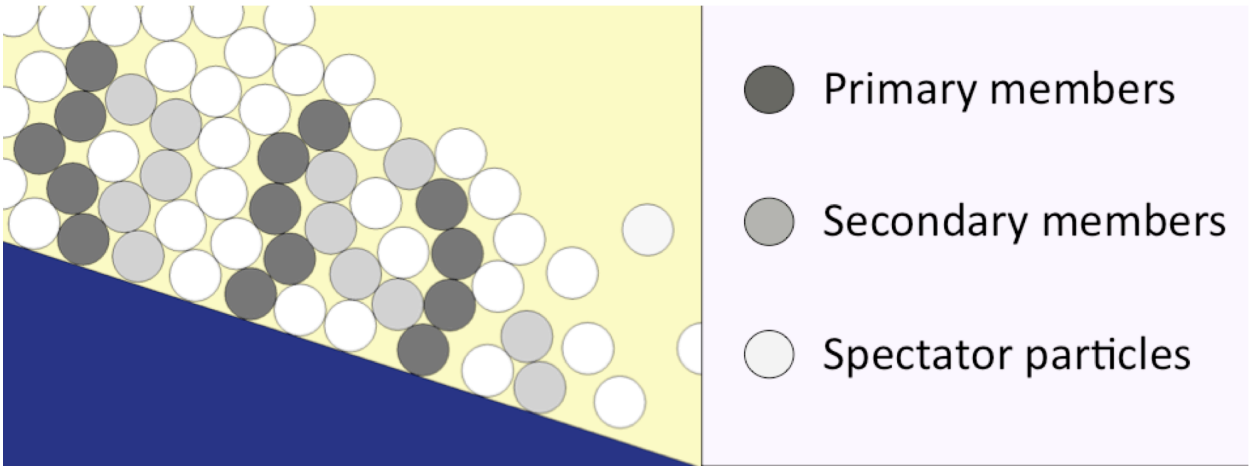

Figure 1. Schematic shows granular flow down an incline. Shaded particles show the filamentary force chain structures formed by inter-particle force propagation that result in a fraction of the particles bearing the majority of body and externally applied body forces. The legend indicates the relative amount of participation in force accommodation by particles in the flow. Primary members are heavily loaded particles, secondary members are marginally loaded particles, and spectator particles are unloaded.

The ability of a granular system to resist deformation is a function of the force chain network formed within the granular system [*Furbish et al.*, 2008; *Sun et al.*, 2010]. The responses of these chain networks to applied stresses ultimately define the material's macroscopic character and influence the transport capacity of these flows [*Dufek et al.,* 2009]. *Furbish et al.* [2008] scaled the production and destruction of force chains with the flow shear rate, and allowed additional destruction caused by acoustic vibrations or grain collisions. *Campbell* [2006] defined granular flows exhibiting force chains as elastic flows. Formulations in the elastic flow theory were derived using a constant volume constraint. Force chains, because they are responsible for anisotropic force distributions in granular media, could carry significant implications for granular

processes in geophysical flows. Localized forces via force chains have been well documented for confined, static and shearing granular systems [*Majmudar and Behringer*, 2005; *Behringer et al.*, 2008; *Muthuswamy et al.*, 2006].

1.1 Volcanic Flows

Understanding of dense volcanic flows, which often start as large blocks that comminute to a mixture of ash (microns) through decameter sized particles, has been closely linked with fundamental studies of granular flows [*Grunewald et al.,* 2000; *Bursik et al.,* 2005; *Dufek and Manga,* 2008; *Kelfoun,* 2011; *Sarocchi et al.*, 2011]. Dense volcanic granular flows can initiate during eruptions (i.e. via dome explosion or edifice collapse) or from flank instability triggered by external factors (i.e. by earthquakes, erosion and flank over-steepening, or meteoric activity) and can form rock falls, debris avalanches, block and ash flows, and pyroclastic density currents [*Huppert and Dade*, 1998; *Grunewald et al.,* 2000; *Bursik et al.,* 2005; *Ponomareva et al.,* 2006; *Dufek and Bergantz,* 2007; *Bernard et al.,* 2008; *Manville et al.,* 2009; *Davies et al.,* 2010; *Thompson et al.,* 2010; *Sarocchi et al.*, 2011]. Debris avalanches generated by volcanic collapse events often lead to secondary flow hazards in the forms of lahars, floods, and tsunamis [*Manville et al.,* 2009], and volcanic flows represent some of nature's most destructive disasters in terms of mortality and property damage [*Huppert and*

Dade, 1998; *Bursik et al.,* 2005; *Thompson et al.,* 2010; *Sarocchi et al.*, 2011].

Despite much work investigating the mobility of natural granular flows, the physics that govern their internal behavior are still poorly understood [*Calder et al.*, 2000; *Grunewald et al.,* 2000; *Crosta et al.,* 2009; *Mangeney et al.*, 2010; *Thompson et al.,* 2010; *Berger et al.*, 2011; *Iverson et al.,* 2011; *Kelfoun,* 2011; *Sarocchi et al.*, 2011]. Gravitational settling and atmospheric entrainment result in enhanced particle concentrations near the bed in pyroclastic flows, and the particle concentration and momentum flux control the destructive force of these flows [*Branney and Kokelaar*, 2002; *Dufek and Bergantz,* 2007; *Ongaro et al.,* 2012]. Three general effects may significantly influence transport capacity and energy transfer within pyroclastic flows: 1. Particle-gas interactions, 2. Particle-Particle interactions, 3. Particle-Bed interactions [*Dufek et al.,* 2009; *Roche,* 2012]. An improved understanding of the pyroclastic flow-bed coupling is desirable for more accurate hazard assessments and interpretation of previous eruption deposits.

1.2 Computational models

Continuum and discrete element method (DEM) numerical approaches have both successfully reproduced many bulk characteristics of dense granular flows. Because many geophysical flows are multiphase, such as pyroclastic flows, debris flows, and landslides, forms of mixture theory have often been

utilized for numerical treatment [*Gray et al.,* 1999; *Denlinger and Iverson,* 2004; *Eringen,* 2004; *Pudasaini et al.*, 2005; *Zanuttigh and Lamberti*, 2007]. Recent depth-averaged continuum models have shown improved simulation of natural and experimental flows through various adaptations; such as modified coordinate systems to accommodate irregular terrain, erosion rate parameters for entrainment, velocity-dependent/depth-independent rheological laws to define basal stresses, and turbulent dissipation terms to account for basal energy losses [*McDougall and Hungr*, 2005; *Pudasaini et al.*, 2005; *Pirulli*, 2010; *Kelfoun*, 2011].

Although continuum models utilizing local depth averaging have exhibited convergence towards the characteristics of natural flows, stress distributions within granular flows down slopes can conflict with local averaging strategies because the rheology depends on transient particle packing [*Bursik et al.*, 2005]. Grain scale anisotropy caused by force chains also cannot be resolved in current continuum approaches. However, flow models that employ grain scale resolution may be able to resolve these localized forces [*Mangeney et al.,* 2007; *Rattanadit et al., 2009; Rycroft et al.,* 2009; *Reddy and Kumaran,* 2010; *Estep and Dufek*, 2012]. Recent studies have indicated that stress fluctuations are only weakly dependant on particle size and flow depth, which counters intuition that fluctuations should decrease as stresses are averaged over a greater number of particles; i.e. an increase in flow depth corresponds to an increase in the number of particles present [*Bursik et al.*, 2005].

Advances in DEM simulations of granular flows, through improved understanding of grain scale processes in granular systems, may lead to constitutive relationships for substrate entrainment in geophysical flows and thus eliminate dependence on empirical parameters to describe entrainment processes [*Estep and Dufek,* 2012; *Estep and Dufek,* 2013]. In DEM simulations each particle in the system is individually tracked and collisions are directly resolved, which is particularly useful for numerical treatment of force chains as well as the long range force transmissions due to force chain activity [*Sun et al.,* 2010; *Estep and Dufek*, 2012]. The discrete element method is generally constrained to small problem sizes because the approach incurs a high computational cost due to the neighbor search algorithms [*Malone and Xu,* 2008]. Despite this limitation, the discrete element method is a useful tool for validation and development of sub-grid models used in continuum approaches [*Garg et al.*, 2010; *Estep and Dufek,* 2013].

Several recent studies have focused on advancing the application of DEM models to granular processes [*Silbert et al.*, 2002; *Boyalakuntla*, 2003; *Brewster et al.*, 2008; *Malone and Xu*, 2008; *Thompson et al.,* 2010; *Sun et al.,* 2010; *Estep and Dufek,* 2013]. Elastic stiffness, energy dissipation, and localized force transmissions for grain-scale force-displacements have been recorded during experiments for various materials, providing information relevant for DEM simulations [*Cole and Peters,* 2008; *Estep and Dufek,* 2012]. DEM simulations employed to investigate granular flow rheological properties showed that contact stiffness may affect the scalings between pressure, strain rate, and shear stress [*Aranson et al.,* 2008; *Estep and Dufek,* 2013]. DEM analyses of the response of

granular flow bulk behavior to varied basal boundary conditions showed that rough bed flows may continue at angles well below the angle of repose, similar to landslides whereby the prolonged motion is enabled by a thin collisional layer near the base [*Silbert et al.*, 2002]. A DEM model that utilized particle bonding to investigate structural evolution and deposit character of volcanic debris avalanches supported initial block sliding and horst and graben emplacement behaviors commonly suggested in the literature, and generated deposit structures that conserved original edifice stratigraphy [*Thompson et al.,* 2010]. These results prompt questions that include how inter-particle and particle-bed force propagation may influence disaggregation, especially in terms of force chain network evolution. Force chain contributions were not evaluated in these DEM studies, however their results imply potential force chain effects.

1.3 Scope of Research

Part 1 of this document discusses material published in the *Journal of Geophysical Research* [*Estep and Dufek*, 2012], and addresses the first questions we investigated with this research: (1) Do the localized forces characteristic of confined granular systems translate to unconfined dynamic systems, and if so are they important for bed forces exerted on the substrates of unconfined gravity-driven granular flows? (2) If force chains are present at the flow boundaries of dynamic granular systems, do the effects from force chains in

unconfined gravity-driven granular flows carry significant implications for erosion and entrainment of the substrate? Such modifications in erosion and entrainment may have implications for enhanced mobility of gravity-driven granular flows [*Berger et al.*, 2011; *Calder et al.*, 2000; *Crosta et al.,* 2009; *Mangeney et al.*, 2007; *Iverson et al.,* 2011]. The entrainment of substrate material by the flowing mass could potentially increase or decrease flow mobility depending on flow dynamics and the physical character of the substrate [*Berger et al.*, 2011; *Iverson*, 1997; *Iverson et al.*, 2011; *Mangeney et al.*, 2010].

The analog experiments, detailed in Part 1, generated two-dimensional, monodisperse, gravity-driven granular flows. Bed force data were acquired using a modified photoelastic technique, and we focused on a simple system to improve our ability to analyze this complex problem. However, with these necessary simplifications we offer the caveat that our experiments and results are not intended to be interpreted as a direct analogue for naturally occurring events. Naturally occurring systems involve complexities that are not addressed by these photoelastic experiments, for example, polydispersity, irregular terrain, pore fluids, and three-dimensional structure; and it is unclear how these results carry over into these more complex regimes. Our experiments represent an end member case of dry granular flow systems. Despite these limitations, our approach allows us to investigate a poorly understood mechanism that contributes to bed physics in natural processes involving granular materials.

Part 2 of this document details work published in the *Journal of Volcanology and Geothermal Research* [*Estep and Dufek*, 2013], and validates a discrete element method (DEM) approach to treat the force chain mechanism and assesses the DEM ability to reproduce localized bed forces from the experimental granular flows of Part 1. This assessment represents a necessary step to evaluating bed forces produced in naturally occurring dense volcanic flows and may give further insight into erosion and re-suspension processes thought to be important in these events [*McDougall and Hungr*, 2005; *Silbert et al.,* 2005; *Mangeney et al.,* 2010]. To investigate the broader implications of this research we also applied the discrete element approach using properties of natural materials to simulate the same type of system employed in Part 1. Although it is unclear how our results of 2D monodisperse granular flows translate to naturally occurring systems, the information presented here provides an important step towards resolving unanswered questions related to bed physics in dense granular flows.

Part 3 of this document discusses the most recent work, which includes the implementation of bidisperse grain populations into the analog and numerical experiments. DEM simulations are also expanded into 3-dimensional domains, an extension that is not feasible using the analog photoelastic technique. Contributions from these additional constraints are evaluated in the purview of peak bed forces derived from force chains. Increased complexity of these experimental granular systems represents progression that approaches natural

systems properties. A verdict of force chain relevance in the bed physics of dense granular flows is delivered in Part 3, which is then concluded with the direction of continued work.

PART 1. ANALOG MODEL

CHAPTER 2. PHOTOELASTIC ANALOG EXPERIMENTS (MONODISPERSE)

The photoelastic method utilizes the properties of transparent materials, such as glass or certain polymers that become birefringent when stressed. When viewed in a field of circularly or plane-polarized light, one can observe the transmission of the internal stresses caused by forces acting on the material boundaries, which is the basis of the photoelastic method [*Majmudar et al.*, 2005]. Birefringence has been used previously, primarily in structural engineering models, to observe elastic stress distributions in small-scale models of structures in polarized light such as dams, bridges, and mechanical components [*Behringer et al.*, 2008]. The same technique can be used to observe the development and evolution of force chains within a sample of a granular material made of transparent particles.

This photoelastic technique provides an avenue for quantitative analysis of force chain networks, because the intensity of transmitted light is proportional to the boundary forces [Figure 2; *Behringer et al.*, 2008; *Majmudar et al.*, 2005]. Figure 3a shows a schematic of the light/lens setup used for our photoelastic experiments, and Figure 3b illustrates the shearing motion of the 2D flows and provides a snapshot image of a transient force chain network. Shearing and compression experiments conducted by *Behringer et al.* [2008], *Majmudar et al.* [2005], and *Sun et al.* [2010] indicate mesoscale (which falls between particle-scale and macro-scale lengths) force propagation in filamentary force chain

networks, in which a fraction of the total number of particles carries the majority of the force [*Geng et al.*, 2003; *Sun et al.,* 2010].

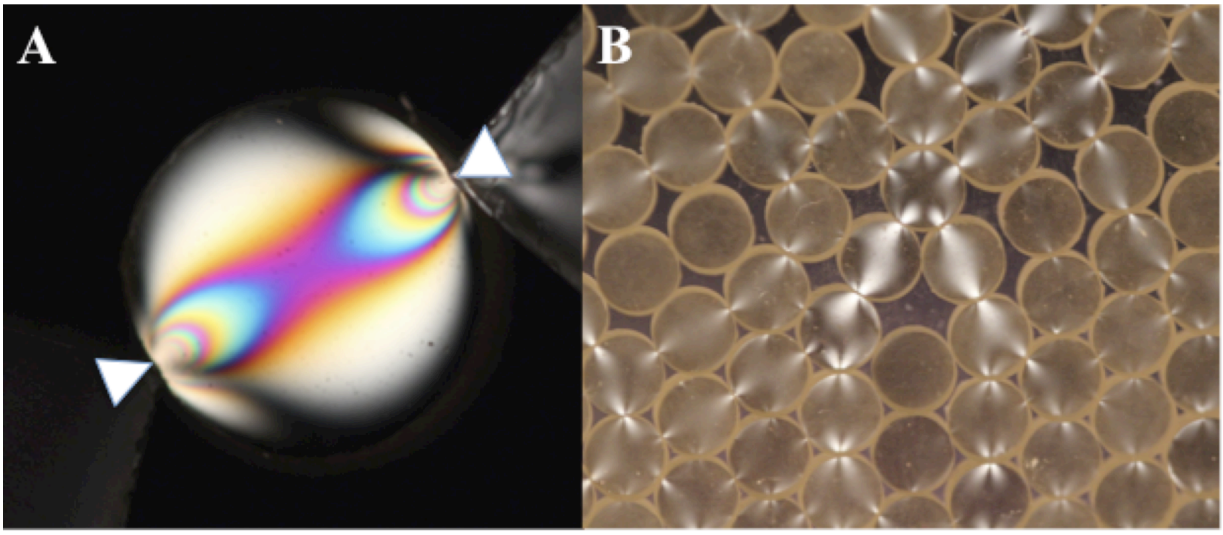

Figure 2. (a) An example of a stress pattern observed on a single photoelastic disk within a force chain, where the white triangles indicate the points of applied force. The lighter filamentary shapes on the disk are fringes, which indicate the magnitude of the strain experienced by the disk – in other words, the fringe pattern can provide an avenue to quantify applied force. (b) An image from one of our experiments of the stressed photoelastic granular material exhibiting force chains. Notice that the fringe order for the disks pictured here does not exceed one, which is a characteristic that continued for the duration of our experimentation.

While force chains have been observed as mesoscale features in length, it is important to note that termination of the force propagation (especially at system boundaries) often occurs over the contact of a single particle (see Figures 2 and 3). The range of birefringence shown by disks in Figure 3 illustrates that a fraction of the disks indeed accommodate system forces, but also that different levels of participation by the disks in the force chain network exist. For example,

disks that are primary members of a force chain exhibit strong birefringence while spectator disks show no birefringence; and secondary force chain members can be identified by minor birefringence (i.e. Figure 1). The levels of participation by force chain members motivate a threshold scheme for analysis, which is described in the calibration section.

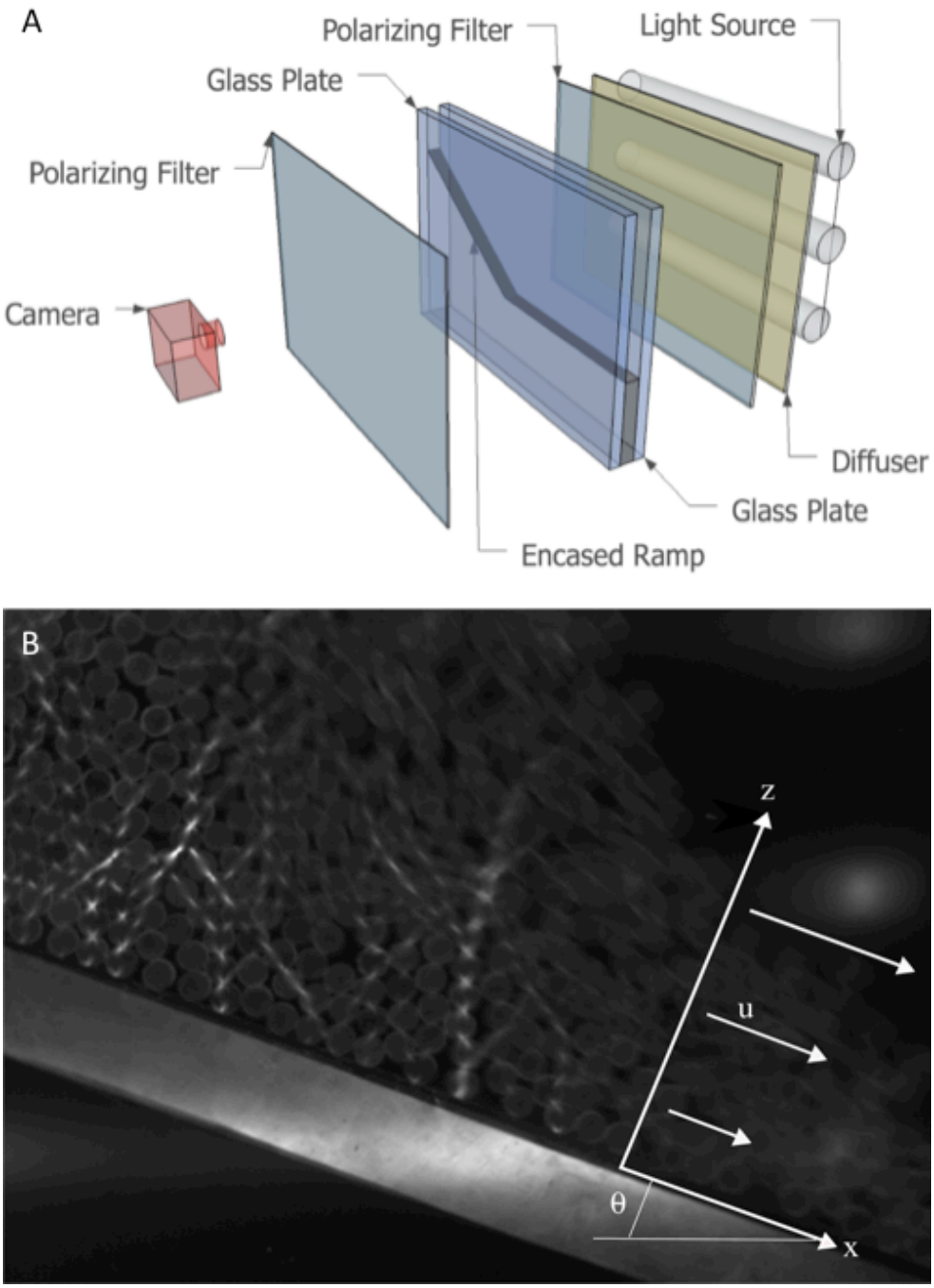

Figure 3. (a) A schematic diagram of the plane polariscope setup used for our photoelastic experimentation. Not depicted here is a collection hopper (shown in Figure 4), which was attached to the end of the apparatus. Images depicted here are not drawn to scale. (b) Snapshot of experimental flow illustrated with inclined x-z coordinate system and shear velocity (u) diagram. The optical activity of the photoelastic disks makes primary force-chain participants, secondary participants, and spectators easily identifiable.

2.1 Experimental Apparatus and Components

To use the photoelastic technique and implement it into our work, we constructed an apparatus to house the material constituting our granular system. Internal structuring for the apparatus consisted of: the release gate, ramp, run-out bed, erodible bed section, retaining wall, and spacers. These parts were constructed from 3.18×10^{-3} m thickness cell cast clear Plexiglass sheets, and 7.62×10^{-5} m thickness clear polyester film sheets by Dupont. Clear glass panes measuring 0.91 m x 0.61 m x 2.38×10^{-3} m housed the internal acrylic members. Delivery and collection hoppers, used for delivery and removal of the granular media from the apparatus, were also constructed from the Plexiglass material. The collection hopper (Figure 4) was attached prior to the onset of the flows, and added 0.30 m to the available horizontal run-out. Two ramp configurations were employed during the experiments: rigid and erodible. The rigid configuration was a straight, rigid bed positioned at a desired inclination. The erodible configuration was similar to the rigid, but included a 0.12 m long x 0.04 m deep rectangular section cut out of the bed, initiated 0.43 m from the upper end of the ramp. Photoelastic disks occupied this cutout area to replicate erodible substrate conditions.

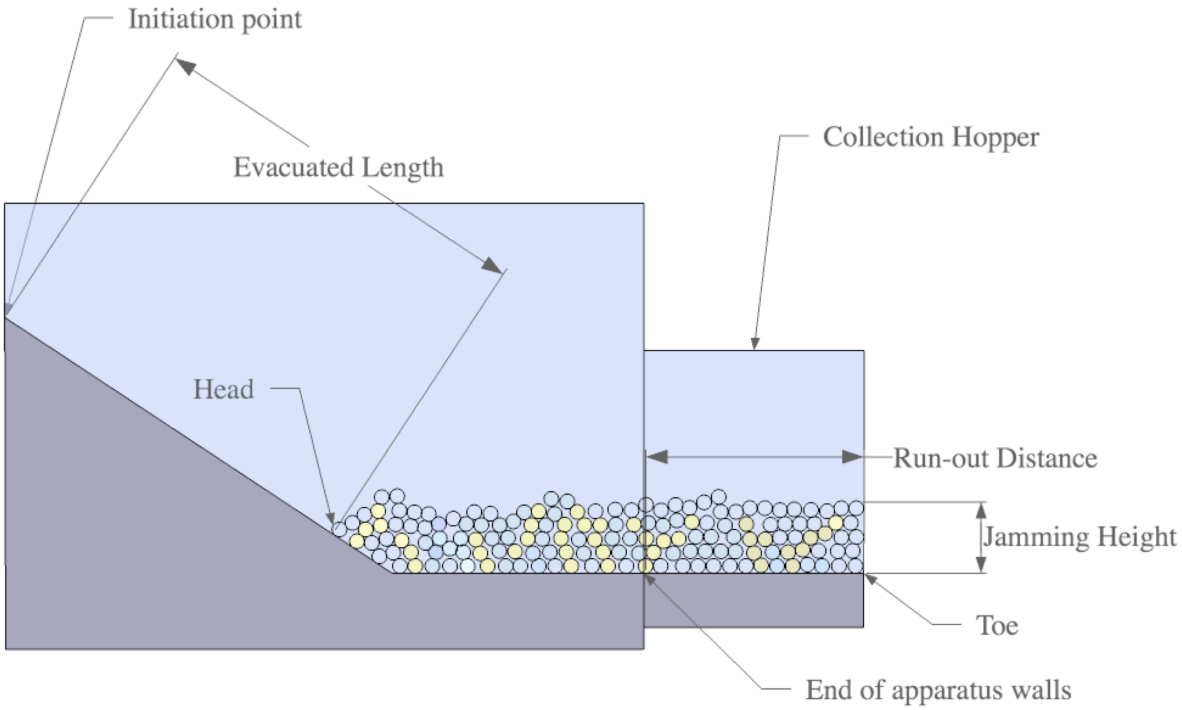

Figure 4. A side view schematic of the experimental apparatus that includes the collection hopper shows a typical flow deposit. Terms used in the text are physically identified. Image is not drawn to scale.

The granular material we chose for our experiments consisted of 6 mm diameter, 1180 kg/m^3 density disks made from Vishay Precision Group's PSM-4 PhotoStress model material. Because of its low elastic modulus and uniform sensitivity character, this material was deemed the most suitable for our experiments. The disks were lightly coated with flour to minimize inter-disk adhesion and disk-wall friction, and from 2100 to 2400 disks were used during each experimental run. We recorded free-fall times from disks inside and outside the apparatus to test for frictional effects due to particle-wall interactions. Free-falling particle velocities inside and outside the apparatus revealed no

determinable difference. We consider wall effects negligible on the basis that estimated particle-wall forces are very small relative to the measured particle-bed forces.

The contact stiffness for the photoelastic disks can be calculated as a function of deformation using the Herztian contact model from the material's Young's modulus, the material's Poisson ratio, and the disk radius [*Coste and Giles,* 1999; *Campbell*, 2006]. Based on the magnitude of particle deformation observed in our experiments we calculated contact stiffness for the experimental disks to fall within a range of 1350 to 2600 N/m. These are low stiffness values relative to those expected for rock or sand, however we believe the expected differences in contact timescales (stiffer particles having shorter contact durations) are not limiting to chain formation and thus force propagation. This argument will be revisited in the discussion.

The coefficients of restitution (ratio of particle velocity after and before an impact) for particle-particle and particle-wall contacts were measured as 0.355 ± 0.121 and 0.473 ± 0.091, respectively. Error values represent one standard deviation for the cumulative data about the mean. These values originate from trials of free falling particles impacting the designated material while being recorded by a high-speed camera. Particle velocities were calculated by dividing particle displacement by elapsed time for sequential images of the frames surrounding the impact. Constraining these restitution values provides an important physical parameter that is necessary for discrete element simulations.

We constructed the plane polariscope (Figure 3a) necessary to visualize force chains present in the granular system. Three 0.36 m fluorescent lights were mounted horizontally in parallel arrangement with 0.08 m vertical spacing, and placed 0.4 m behind the back glass pane of the apparatus. Rosco Laboratories linear polarizing film and diffuser sheets were mounted between the apparatus and the light setup. On the face of the front glass plane of the apparatus was a second polarizing sheet, oriented with orthogonal polarity relative to the larger backside polarizing film. The position of the polarizing films and diffuser were adjusted to frame the area of interest for individual experimental runs. Each experiment was recorded at 200 fps by a Miro Phantom high-speed camera, equipped with a Pentax CCTV 50 mm lens, and positioned 0.55 m from the front glass pane of the apparatus (opposite the lighting arrangement).

2.2 Photoelastic Implementation

We conducted a suite of experiments consisting of 24 individual flows. Three ramp inclinations, 10, 20, and 30 degrees, were employed for both the rigid and erodible bed sections. For the rigid bed case we used two focus areas: one was centered on the release gate, and a second was located down slope, and centered 0.185 m before the terminal end of the apparatus. Four flows were initiated at each inclination (two per focus area). After each run we measured and

recorded run-out distance at the terminus, evacuated distance from initiation point, and jamming height at the head and toe of the flow deposit (Figure 4). Run-out distance is the horizontal distance the flow reached beyond the apparatus walls and into the collection hopper. Evacuated length is the down-slope distance between the flow deposit and the retaining wall at the top of the flow initiation point. Jamming height at the head and toe describes the height of the flow deposit at the retaining wall located above the flow initiation point and the terminal end of the retention hopper, respectively. For flows exhibiting evacuated length, no jamming occurs at the head of the deposit. Accordingly, for flows exhibiting run-out distance less than 0.30 m, no jamming occurs at the toe of the deposit. The high-speed imagery captured during the experimental runs provided a means of recording flow duration, bed forces, chain counts, chain lengths, chain frequency, and fringe orders (force magnitudes). For the erodible bed case we also used two focus areas: the first was the same as for the rigid bed experiments, and a second framed the erodible bed section down-slope from the release gate. Four flows were run at each inclination for the erodible bed case, two for each focus area. Force propagation distance and magnitude into the bed material was measured for the erodible bed experiments.

A feed hopper was used to deliver the disks into the experimental apparatus for each experiment. The hopper was attached to the top of the apparatus, and the particles were released into the upper part of the housing. In this way the particles self-aligned into a random arrangement, and formed a

static granular system confined by the release gate. Once loaded, the disk arrangement was recorded. Due to the monodisperse nature of the system, the initial packing arrangements often exhibited some unmeasured degree of crystallinity (apparent order in packing). Flow motion was initiated by rapid removal of the release gate, which allowed the collapse of the static disk structure and resulted in an unconfined, gravity-driven, dense granular flow. High-speed video recorded the experiment, and the final deposit was recorded with a still image.

Still frame images from the high speed recordings of each incline – bed pairing were used to evaluate localized (force chain) versus averaged (from flow height) bed forces, and to determine the correlations between bed force orientations with chain inclinations relative to the substrate and total bed force magnitudes. Criteria for the image selections were clarity of force chains, fringe patterns and disk morphologies, as well as visibility of the granular flow surface in measurable proximity to the substrate.

2.3 Photoelastic Calibration

In order to quantify the force magnitudes carried within the observed force chains, a proper calibration of the force-strain relationship was necessary. Conventional low elastic modulus PhotoStress calibration is achieved by an

imposed-curvature method [*Vishay*, 2010]. For most PhotoStress coated surfaces, the traditional approach to photoelastic calibration is to impose a series of known strains on simply shaped (typically a beam or rod) material with photoelastic coating, record the applied force and resultant fringing, and use this information to quantify the strain and/or force to the more complex structure under investigation. Multiple fringe cycles (a fringe order greater than one) indicate rather large forces relative to the elastic modulus of the photoelastic material. For fringe orders less than one, the affected, or optically active, area of the photoelastic material increases with increased strain. However, when the fringe order exceeds one, the area of birefringence no longer requires growth. Instead, the fringe pattern may cycle within the same area (see Figure 2). This is especially true when the optically active area considered is the entire surface area of the investigated material.

Our experimental granular systems possess unique characteristics, which allow us to justify an alternative calibration technique for our work. Most importantly, the relatively small-magnitude forces in our experiments never produce fringe orders greater than one. This is due to the small size and density of the disks, and the small scale of the granular systems employed. The discrete, monodisperse character of the disks along with the limited fringing observed means that the area of optical activity on a given disk is proportional to the force imposed on the boundaries of the disk. We use this relationship as a

proxy for an incremental calibration scheme that correlates contact forces with area of optical activity.

Four threshold fringe magnitudes that encompassed the spectrum observed during the experiments were established and systematically reproduced: zero – no visible fringing; contact (or quarter) – fringe initiation at the contact point on disk boundary; half – fringe propagation reaches midway through a disk; and full – fringe propagation covers the full diameter of a disk. Figure 5A shows a schematic diagram of the calibration setup. A 2D hopper, used as an alignment guide for the disks, was suspended 0.003 m above the surface of a digital scale. Four disks were placed on the scale in a double layer arrangement, and their cumulative weight recorded; this constituted the 'zero fringe' case. The double layer allowed for clear visibility of fringing, which is necessary for imaging and accurate reproduction of fringe magnitudes. A dSLR camera was used to image the calibration sequences. A manually controlled acrylic arm applied force to the upper disk until the appropriate amount of fringing was produced, and the scale weight reading was recorded. This method was repeated for each of the threshold fringe magnitudes, ten times each. The scale-weight readings were converted to force units that were normalized for an individual disk experiencing force applied at one point of contact by dividing the zero-fringe value by the number of disks used in the calibration setup. Subtracting the residual, self-applied force caused by the disk weight was the final refinement of the calibration data. Figure 5B shows the calibration results.

The calibration data, although discrete to threshold values, encompass the magnitudes of fringing observed throughout the suite of our experiments. Owing to this fringe containment and the small optically active area (relative to the facial area of a disk) available between threshold fringe levels, a simple linear interpolation between calibration data points is reasonable. We define a quantity, the fringe factor, which is the fractional area of a disk that is optically active; for example, if a disk has a fringe factor of 0.5, then half of its facial area is optically active. Table 1 compares calibration fringe thresholds to the number of self-weighted disks required to generate a force equivalent to each fringe threshold.

Table 1. Applied force and equitable disk weight in terms of calibrated fringe threshold values

Fringe Threshold	Number of Disks to Equal Applied Force	Force Applied During Calibration (N)
None	1	0.001
Contact	9.55	0.009
Half	36.68	0.036
Full	70.34	0.068

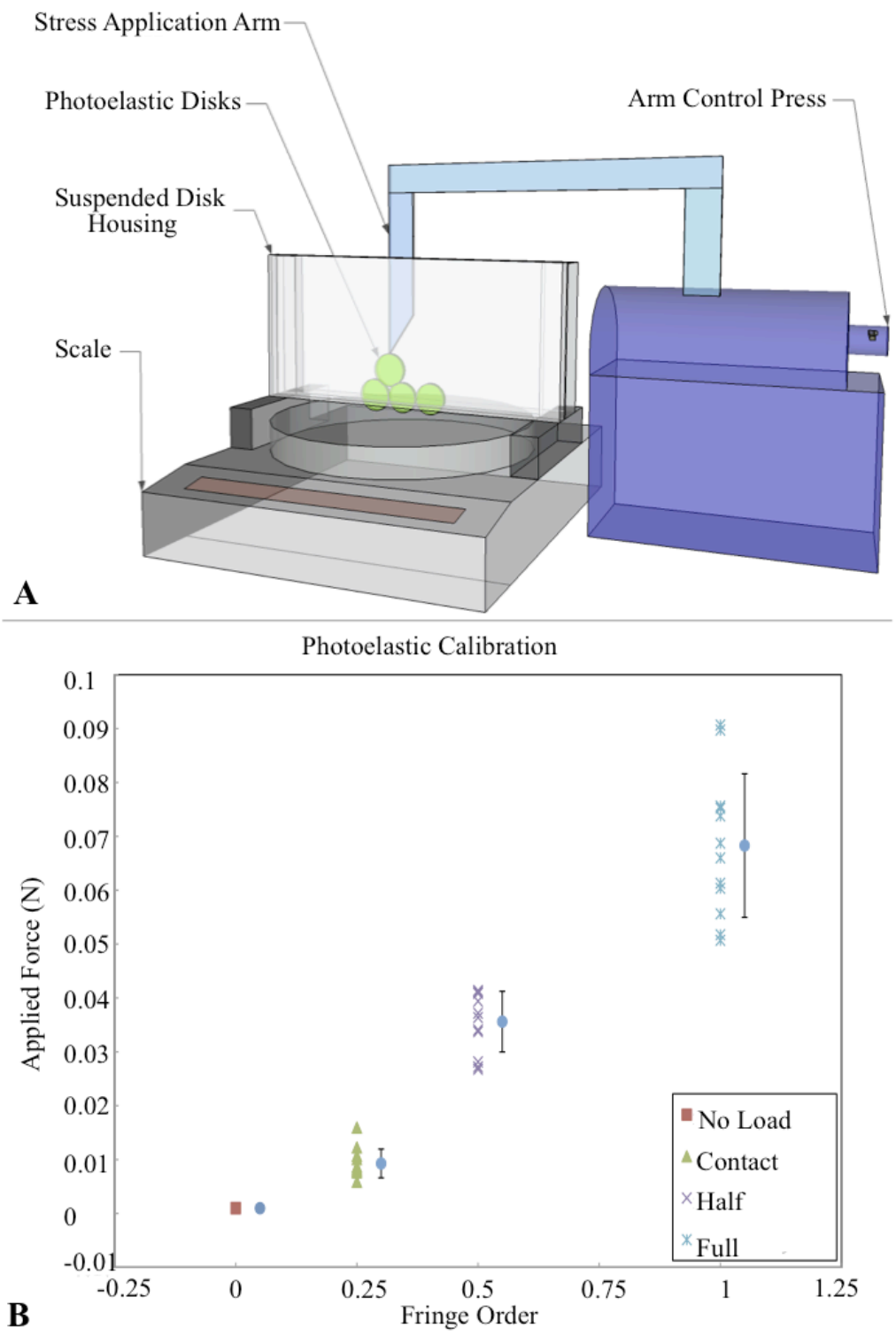

Figure 5. (a) Schematic view of the calibration setup used during our experimentation. An acrylic arm applies force to a photoelastic disk until the desired fringe magnitude is reached. The underlying digital scale records the weight change; which is used to calculate the applied force. (b) Plot shows the

calibration results in terms of fringe threshold values. Since the fringing observed during experimentation falls within the bounds of our calibration data, interpolation between the discrete threshold values is justifiable. Note that the mean data points and deviations bars are offset so they are distinguishable from standard data.

2.4 Image Processing

Information from the calibration-sequence images was implemented into an image-processing algorithm that we developed using MATLAB's image analysis tools to extract data from the experiments. Individual frames from the video clips of each run were parsed into sequential tiff images. The image sequences were processed through the program, which identified the force chain fringe patterns and converted them into binary form, filtered the magnitudes by fringe thresholds, and computed several parameter values for the selected force chains. The program saved output files containing force chain counts, average and total chain lengths, and respective bed force magnitudes.

CHAPTER 3. PHOTOELASTIC RESULTS

Flow durations for each incline, recorded as the time elapsed between flow initiation and establishment of a static deposit, were: 10º slope, 1.74 ± 0.16 s; 20º slope, 2.18 ± 0.13 s; and 30º slope, 2.62 ± 0.21 s. Table 2 provides measured deposit values for several physical parameters depicted in Figure 4. External files Media 1 and Media 2 show video examples of rigid bed and erodible bed experimental granular flows, respectively.

Table 2. Dimensional measured values for flow deposits.

	Rigid		
Incline	10º	20º	30º
Run-out Distance (m)	0.041 ± 0.028	0.162 ± 0.026	0.300 ± 0.000*
Evacuated Length (m)	0.000 ± 0.000	0.000 ± 0.000	0.056 ± 0.028
Jamming Height @ Top (m)	0.186 ± 0.002	0.099 ± 0.003	0.000 ± 0.000
Jamming Height @ Bottom (m)	0.000 ± 0.000	0.000 ± 0.000	0.009 ± 0.003
	Erodible		
Incline	10º	20º	30º
Run-out Distance (m)	0.069 ± 0.029	0.153 ± 0.010	0.278 ± 0.021
Evacuated Length (m)	0.000 ± 0.000	0.000 ± 0.000	0.014 ± 0.022
Jamming Height @ Top (m)	0.187 ± 0.012	0.130 ± 0.002	0.005 ± 0.001
Jamming Height @ Bottom (m)	0.000 ± 0.000	0.000 ± 0.000	0.002 ± 0.003

[a]The available run-out distance in the collection hopper was 0.30 meters; therefore this represents a minimum value.

Bed force time series reveal irregular distributions of discrete localized bed forces for each incline in both time and magnitude. The bed-force time series are presented in Figure 6 for each inclination of the rigid bed experiments. The data, a summation of localized (force chain) and averaged (flow height) bed forces, focus on the bed forces within an approximately 0.012 m length section on the ramp surface over the duration of each flow. These time series show bed forces at one position on the substrate as the flow passes. Visual inspection of the active flows also revealed irregular spatial force chain distribution patterns.

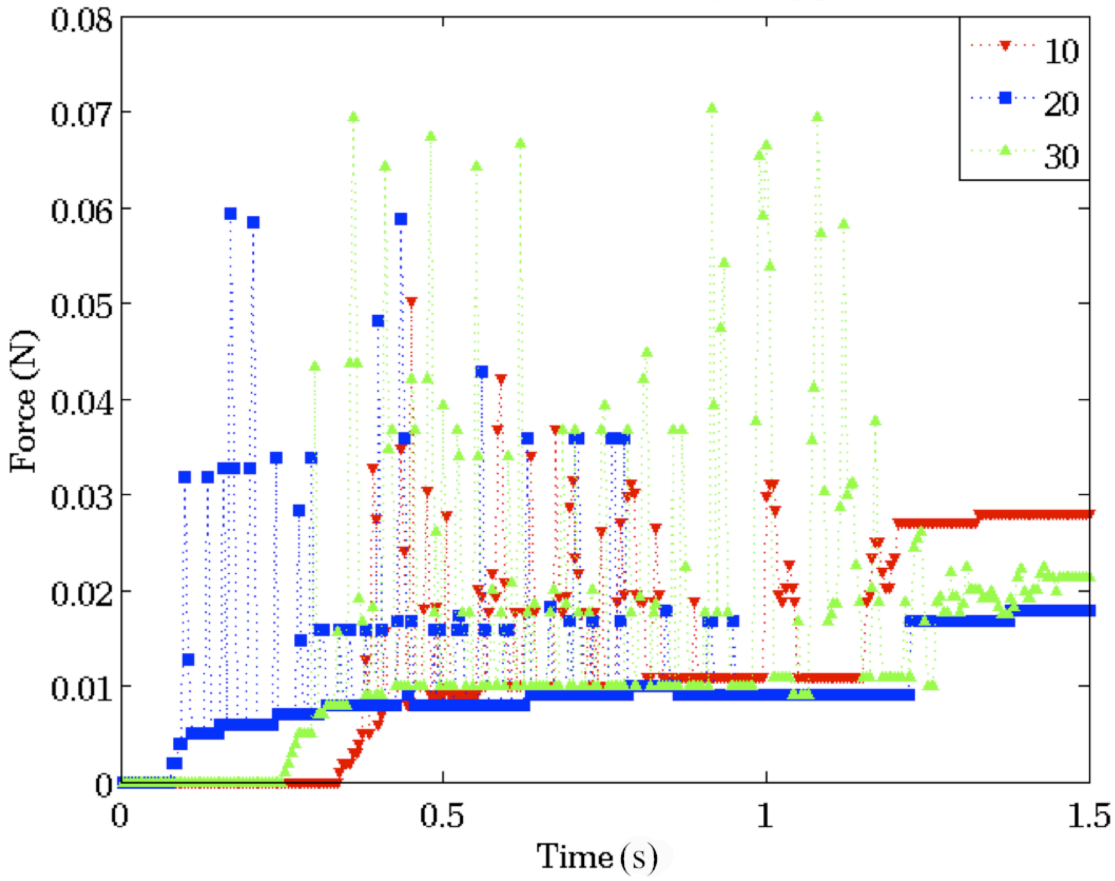

Figure 6. Bed force time series describes cumulative bed force magnitudes due to force chains combined with the flow body for each inclination during rigid case runs. Red inverted triangles, blue squares, and green triangles represent the 10-degree, 20-degree, and 30-degree cases, respectively.

Peak forces imparted by force chains on the bed greatly exceeded mean forces due to the flow thickness, demonstrated in Figure 7. The mean local bed force, the time-averaged value of the measured localized bed force magnitudes, was obtained from analyzing the fringe factor of the chain member contacting the substrate. The time-averaged flow height bed force was estimated from the height of the flow normal to the force chain-substrate contact point to give a point

of comparison with those forces we would predict from a depth-averaged perspective (i.e. to compare the results to depth-averaged continuum models as a base-line).

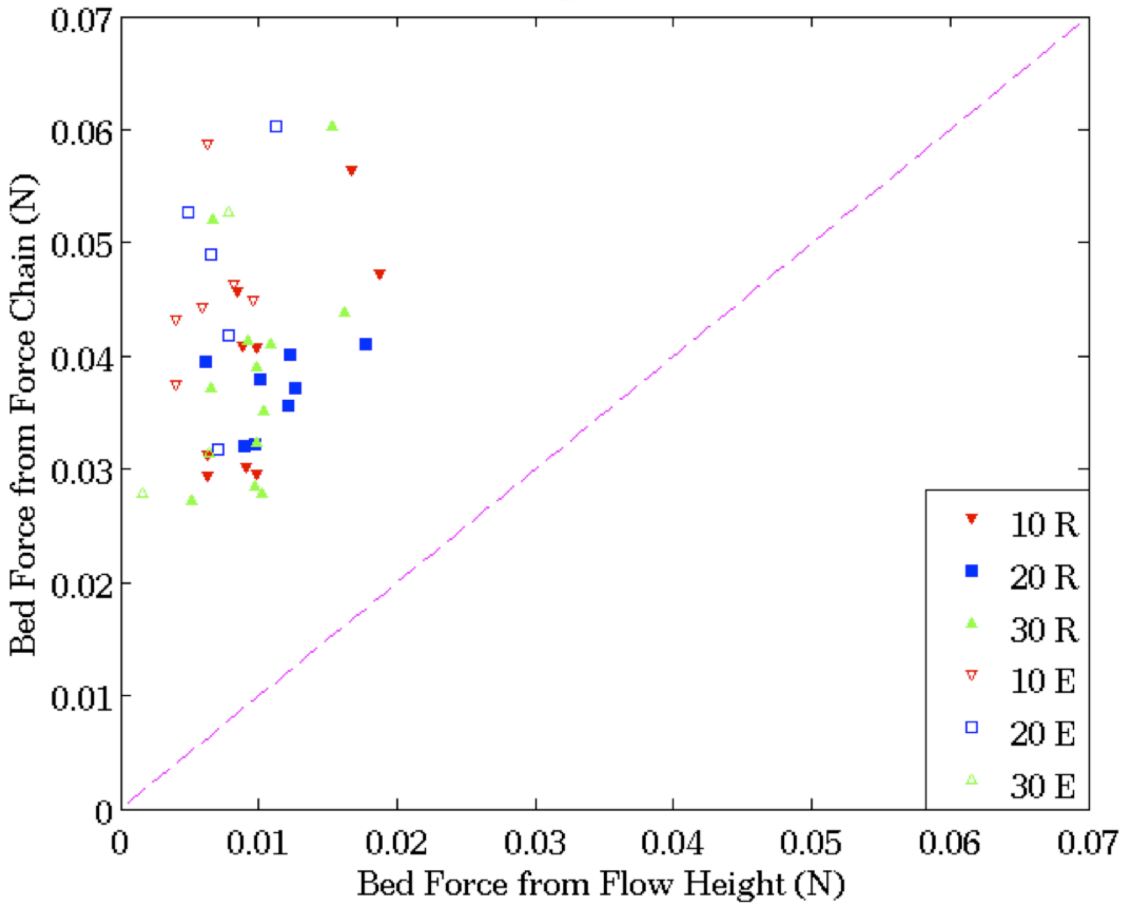

Figure 7. Localized bed force magnitudes from force chains compared to averaged bed force magnitudes calculated from flow body height for rigid and erodible cases. The dashed line illustrates equity between force types, which emphasizes the significant force localization. Red inverted triangles, blue squares, and green triangles represent the 10-degree, 20-degree, and 30-degree cases, respectively. Solid markers indicate rigid bed data (denoted by 'R' in the legend) while open-face markers indicate erodible bed data (denoted by 'E' in the legend).

Depth-averaged continuum models [*Denlinger and Iverson,* 2004; *Gray*, 1999; *Vreugdenhil,* 1994] often calculate normal bed stresses by assuming that vertical stresses are dominated by weight of the flow immediately above the bed. In addition, *Denlinger and Iverson* [2004] proposed that a fluctuating vertical acceleration term is needed to account for the equivalent of down-slope and centripetal acceleration for flows over complex three-dimensional topography. The flow height bed force we report here is an estimated value used to reference the order of magnitude we expect from depth-average continuum models for normal bed forces. Localized (force chain) bed force relative to flow height bed force magnitude was 435.62 ± 0.59 % for rigid bed conditions and 738.32 ± 0.57 % for erodible bed conditions. Error values represent one standard deviation for the cumulative data about the mean.

Photoelastic disks occupying the cutout area in the erodible-bed show an elastic feedback response to the flow body during flow-substrate interaction, which enhances the flow-bed contact forces. The material in the erodible bed section communicates with the flow body through extended force propagation. Because this extension is not reflected in the flow height bed force values (the flow height does not increase), the localized bed forces for the erodible section are significantly higher than the rigid case. On the basis of 29 rigid-bed and 14 erodible-bed images, the localized force values include results from both focus areas of the experiments. Although the precise value of the averaged localized force is a result of the particular location chosen for the measurements and the

geometry of the apparatus, our results indicate that considerable bed force excursions due to force chain development are likely in an unconfined, gravity-driven granular flow.

We observed ejection of bed particles by the flow at each ramp inclination, with a positive correlation between the number of ejected particles and ramp inclination (higher inclines had more ejected bed particles). During the two separate flows at each ramp inclination, the total number of ejected bed particles was 1, 5, and 27 for the 10-degree, 20-degree, and 30-degree ramp inclinations, respectively. Each ejected particle was entrained into the body of the granular flow. Deposition of flow particles into the erodible bed section after bed particle ejection was also observed but not quantified.

Near steady state conditions for chain lengths are reached quickly relative to flow duration (after ~0.5 s the chain length values show little variance). Figure 8A and B presents time series showing 2 second durations of average length, total length, and number of force chains for each incline from rigid bed and erodible bed experiments, respectively. No distinguishable patterns were recognized upon analysis of the chain length and number regressions. Because the area captured by the camera frame was limited, data presented in the time series plots are representative of a fraction of the flow body.

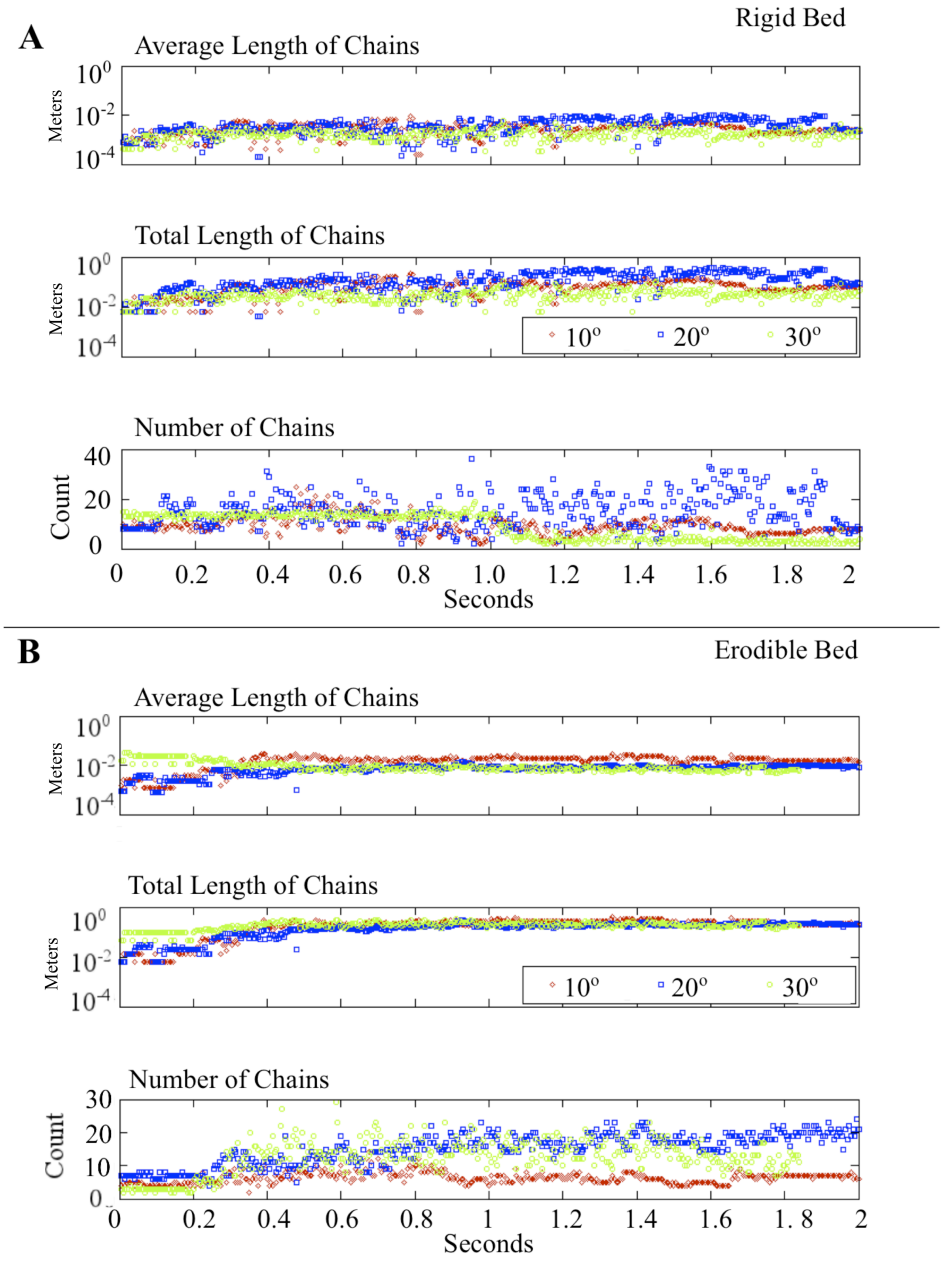

Figure 8. (a) Time series of average length, total length, and number of force chains for each incline from rigid bed experiments. (b) Time series of average length, total length, and number of force chains for each incline from erodible bed experiments. Red diamonds, blue squares, and green diamonds indicate 10-degree, 20-degree, and 30-degree ramp inclinations, respectively.

Using the Pearson product-moment method [*Dutilleul et al.,* 2000; *Trauth*, 2007], no significant correlation was found between force chain inclinations and the components (normal and shear) of the bed forces. Although no strong correlations were discovered, the chain inclinations and total bed force magnitudes showed small positive correlations; whereas the normal versus shear components displayed a medium negatively correlated relationship. Chain inclinations describe the force chain angle proximal to and relative to the flow substrate. *Trauth* [2007] provided a detailed description of the Pearson product-moment method, which measures the strength of linear dependence between two variables.

Because photoelastic material was used for the erodible-bed section, our experiments provided an avenue to investigate bed force propagation into the substrate. Employing the same techniques used to determine bed forces at the flow-substrate interface, we recorded the extent of birefringence observed in the cutout bed section resulting from flow contact with the substrate. Propagation extent versus bed-force magnitude is plotted in Figure 9. Propagation was limited by edge effects of the section domain so that the represented values are minimum values. The data for the bed-force propagation show no significant correlation between applied force and propagation extent, as the correlation coefficient of 0.328 is much lower than the 0.532 minimum value required for significance at the 95% confidence level at the given sample size. We find evidence of birefringence in the substrate ahead of the flow front due to forces

applied upslope by the flow (Figure 10).

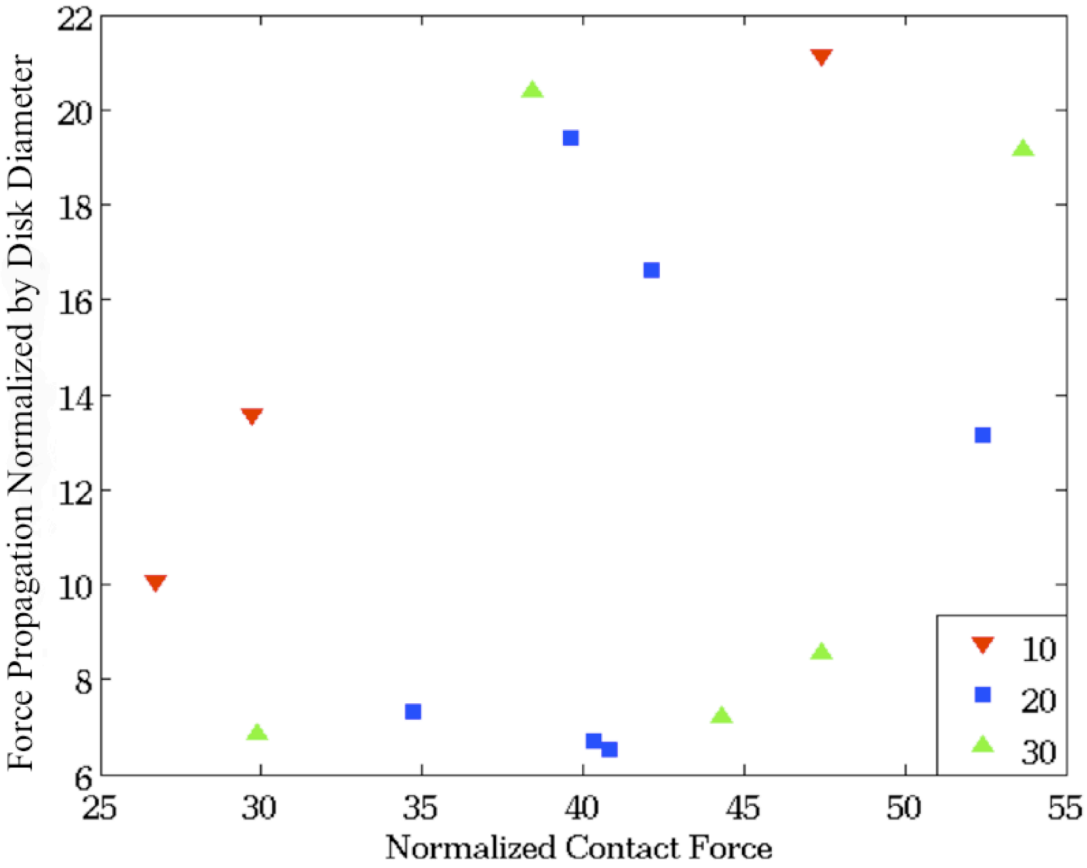

Figure 9. Extent of force propagation into the erodible bed section is shown, where length is normalized by the diameter of a disk. Normalized contact force refers to the magnitude of bed force at chain-bed contact point for each ramp inclination where force is normalized by one particle's gravitational acceleration.

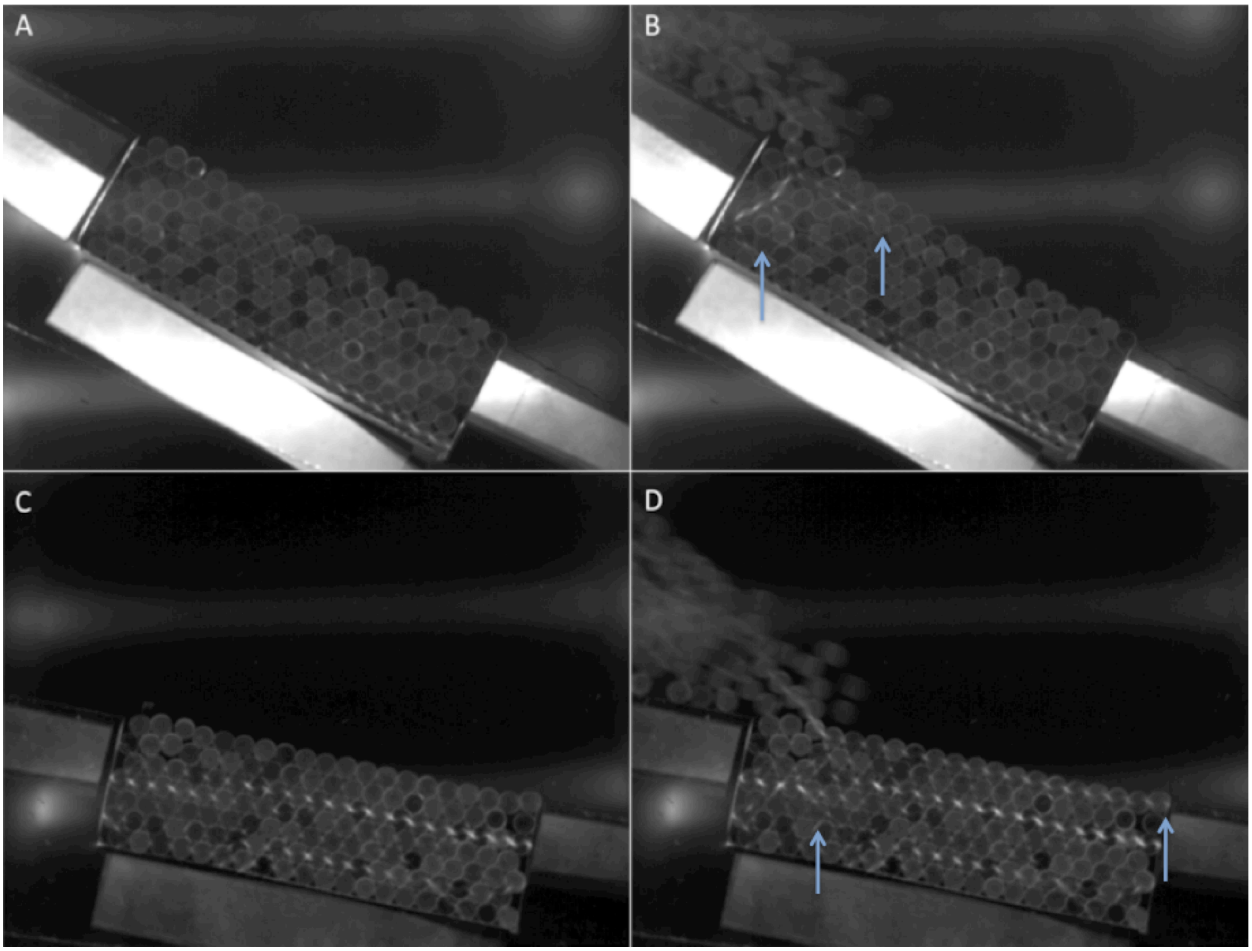

Figure 10. Images of the erodible bed section show force propagation into the bed section, and ahead of the flow front. The top two pictures (A, B) are the 30 degree case, and the bottom two pictures (C, D) are the 10 degree case. The left column (A, C) shows the bed sections before the flow impacted them, and the right column (B, D) shows the flows contacting the erodible bed sections. The propagated forces are shown by the altered birefringence of particles in the erodible bed section, and are pointed out by blue arrows.

CHAPTER 4. PHOTOELASTIC DISCUSSION

Our experiments provide clear evidence of extreme localized (force chain) bed forces relative to average (from flow height) bed forces, considering 'extreme' to be greater by at least an order of magnitude. This work highlights that force chains, even in low-slope flows, can produce particle chain networks that may initiate stresses exceeding critical shear thresholds and may contribute to entrainment in granular systems. Traditional continuum models that derive averaged bed force values currently do not address the contributions of force chains to the flow substrate, and thus may under-predict bed forces locally. However, flow models that employ grain scales may be able to resolve these localized forces [*Mangeney et al.,* 2007; *Rattanadit et al., 2009; Reddy and Kumaran,* 2010; *Rycroft et al.,* 2009].

Force chain processes at the beds of granular flows likely contribute to the mechanism of entrainment through either physically ejecting grains due to the localized forces, as seen in our experiments, or by modifying bed conditions. *Schuerch et al.* [2011] used a combination of estimated maximum flow depths with elevation changes to evaluate the effect of flow depth on the probability of erosion in debris flows. The work shows that substantial erosion is more likely with increased flow depth, but also that a wide range of outcomes is possible at any given flow depth. For most debris flows, flow depth is largest at the front of the flow, and flow depth influences forces acting on the channel bed by way of

three mechanisms: (1) increased basal shear stresses, (2) the impact stresses of coarse particles in the flow front, and (3) hydraulic pressure at the flow front [*Schuerch et al.,* 2011]. *Iverson et al.* [2011] observed a positive correlation between water content of the substrate and scour depth for large scale experimental debris flows, and *Schuerch et al.* [2011] noted that coarse debris flow fronts have very low fluid pressures. The influences on the bed physics of fluid interactions within granular flows are beyond the scope of this work, however low pore pressures at flow fronts may allow granular processes such as force chains to operate more effectively. Although not evaluated in these experiments, the propagation of force chains into the subsurface below and in front of the flow may also aid entrainment by modifying pore pressure in those substrates that are at or near liquid saturation.

If a force chain is oriented obliquely to the bed it contacts, which was commonly observed in our experiments, then the force transmitted to the substrate by that chain contains normal and shear components. Interestingly, in our experiments the shear bed force components derived from force chains carried the same order of magnitude as the normal bed force components for the chain inclinations observed. This further supports the assertion that force chains in granular flows may contribute to the shearing mechanism necessary to 'pluck' substrate material, initiate entrainment, and potentially alter flow momentum. This is not to say, however, that force chain dynamics are the only mechanism contributing to substrate entrainment in natural in granular flows.

Similarity in threshold behavior for substrate entrainment for unrelated systems occurs because entrainment thresholds depend on entrainment inducing bed forces themselves, and not on the agent producing the forces. Granular flow and fluvial flow systems may both exhibit critical threshold phenomena for substrate entrainment [*Ancey et al.*, 2008; *Arulanandan and Perry*, 1983; *Garcia and Parker*, 1991; *Frey and Church*, 2011; *McDougall and Hungr,* 2005; *Sarmiento and Falcon*, 2006]. It is unclear whether the basal shear stresses in granular flows are analogous to a critical shear stress for fluvial or other fluid entrainment processes, as other effects such as grain impacts or water content are likely relevant [*Schuerch et al.,* 2011; *Iverson et al.,* 2011]. Previous work showed the similarities between granular and fluvial bed load systems [*Frey and Church*, 2011; *McDougall and Hungr,* 2005], suggesting that comparable physics may dominate each of these regimes. Force chains may supply a viable mechanism capable of producing shear forces necessary for entrainment in granular systems.

Our experiments also indicate significant propagation of bed forces into the flow substrate, which is also a result of dynamic force chain processes. Although limited due to edge effects of the experimental apparatus domain, our data suggest that bed forces applied during force chain contact with the bed can propagate on the same length scales as force chains within the flow body. It is important to note that the limited domain size in our erodible bed experiments resulted in near-crystalline particle arrangements in the bed. Examination of

static granular systems has shown that increases in disorder correlate to decreases in force propagation [*Geng et al.*, 2003]. However, *Geng et al.* [2003] also reported that long-range force correlation for anisotropies in granular systems are caused by shearing motion. For force chains contacting the bed near the flow front, our experiments demonstrate that the bed forces may propagate ahead of the flow front and affect the substrate particles before the flow body reaches their proximity. This may potentially influence pore pressures in front of the flow in the case of wet substrates. Because force chains can cause significant perturbations to the forces at the bed, this work suggests that sub-grid models (varied spatial resolution) may be necessary when applying continuum models to granular flow erosion problems. Furthermore, our results imply that discrete-element computations may be particularly useful in examining force chain processes in geophysical flows [*Schwaiger and Higman*, 2007; *Aharonov and Sparks*, 2004].

The low contact stiffness of the material we employed in our experiments relative to natural material raises questions concerning the applicability of our results to natural systems in terms of force chain stability due to an expected reduction in contact times for stiffer particles. *Campbell* [2003] showed that force chain stability in confined systems is dependent on confining pressure, restitution coefficient, and chain length. From this description, force chain stability in confined systems results from a balance of confining pressure and loading on the constituent particles within the chain. With the approach of *Campbell* [2003] force

chains with ‘unloaded’ contacts are unstable because one end of the chain is unconfined.

However, force transmission via force chains does not require that the chains remain stable for long periods of time. Indeed, our experiments reveal significant force propagation through chains that persist for at most the duration of one high-speed video frame (1/200 sec). Because our temporal resolution is 1/200 sec, we cannot definitively say that force chains captured in our images persist even for that long. Our data clearly indicate that force chains provide localized forces to the substrate, but we can use the granular time scales presented by *Sun et al.* [2010] to better illustrate why this occurs. Three granular time scales are defined: t_m – microscopic time scale, t_c – macroscopic time scale, and t_R – Rayleigh (mesoscopic) time scale. The microscopic time scale

$$t_m = \frac{d}{\sqrt{\frac{P}{\rho}}} \qquad (1)$$

denotes the time for particle displacement (with density (ρ)) over the distance of a particle diameter (*d*) subjected to local pressure (*P*), which is the typical time scale of particle rearrangement. The macroscopic time scale

$$t_c = \frac{1}{\gamma} \qquad (2)$$

is linked to the contact lifetimes during the particle rearrangements occurring during a flow with shear rate (γ). The Rayleigh (mesoscopic) time scale

$$t_R = \frac{\pi d}{0.163\nu + 0.877}\sqrt{\frac{\rho}{G}} \qquad (3)$$

is the time for a Rayleigh wave to propagate along a particle surface with Poisson's ratio (ν) and shear modulus (G). The mesoscopic time scale represents the time for an elastic wave to propagate through a particle contact, i.e. force propagation.

Calculating these characteristic timescales for the disks in our experiments, and assuming a force chain consisting of 10 disks we find: $t_m = 6.52 \times 10^{-3}$ s, $t_c = 6.25 \times 10^{-2}$ s, and $10^* t_R = 5.85 \times 10^{-3}$ s. Table 3 presents the parameter values used in the time scale calculations. Force propagation occurs over a shorter time period than the lifetime of particle contact or particle rearrangement, which indicates that the force chains effectively instantaneously transmit forces relative to other flow processes. This also illustrates that contact times do not scale with particle stiffness in dense granular flows, alternative to the trends observed in systems dominated by binary collisions.

Table 3. Parameter values used for granular time scale calculations

Time scale	**$t_m = 6.52 \times 10^{-4}$ s**		**$t_c = 6.25 \times 10^{-2}$ s**		**$t_R = 5.85 \times 10^{-4}$ s**	
Parameter	d	ρ	P	γ	G	ν
Value	0.006	1180	1000	16	1.3×10^6	0.5
Units	m	kg m^{-3}	Pa	s^{-1}	Pa	n/a

4.1 Photoelastic Experiments Conclusions

Photoelastic experiments provide quantitative evidence of dynamic force chain activity in gravity-driven granular flows, and reveal the significance force chain activity carries for conditions at the flow substrate. This work demonstrates that force chains, regardless of their stability, transmit high magnitude localized forces to the substrate of dense granular flows. Our experiments provide a dataset to validate discrete-element granular flow models both qualitatively and quantitatively. Inter-particle force and bed-force data provide constraints on force magnitudes, and images obtained from the experiments reveal geometric information in both spatial and temporal domains. Future experiments of this type may increase scale sizes for the experimental systems, which would be especially useful for the erodible bed case. A larger erodible bed section may eliminate the observed edge effects and allow for more amorphous substrate particle arrangements. Polydispersity within the granular media and addition of fluids into the system are planned to strengthen experimental applicability to natural systems.

PART 2. COMPUTATIONAL MODEL

CHAPTER 5. DISCRETE ELEMENT NUMERICAL METHODS

Our model for this work utilized the Multiphase Flow with Interphase eXchanges – Discrete Element Model (MFIX-DEM) open source code, a product of the National Energy Technology Laboratory [*Garg et al.,* 2010]. The open source MFIX–DEM code can be used for discrete element method, continuum discrete method, and two-fluid method simulations from a single source code; however the current work focuses on purely granular systems and therefore uses only the discrete element portion of the code base. In the MFIX–DEM code the solid phase is represented by individual particles and the collisions are directly resolved using the soft-sphere approach of *Cundall and Strack* [1979], which is based on a spring-dashpot model. The soft-sphere approach is appropriate here since it relaxes the binary collision assumption of the hard-sphere approach and thus allows for multiple particle contacts. Additionally, the soft-sphere approach is advantageous in that the required time-step is dependant on contact stiffness and independent of packing fraction [*Garg et al.,* 2010].

In the DEM approach, the m^{th} solid phase is represented by N_m disk-shaped particles with each particle having diameter D_m, thickness h_m, and density ρ_m. Since the current work is concerned with monodisperse granular flows only one solid phase is considered. We note that as we are comparing our calculations to 2D experiments the particles we considered were truly disk shape and not spheres, and the numerical approach was modified accordingly. The *N*

particles occupy a Lagrangian reference frame at time t by $\{\mathbf{X}_i(t), \mathbf{V}_i(t), \boldsymbol{\omega}_i(t), D_i, \rho_i, i = 1,...,N\}$, where $\mathbf{X}_i(t)$ represents the i^{th} particle's position, $\mathbf{V}_i(t)$ and $\boldsymbol{\omega}_i(t)$ express linear and angular velocities, D_i symbolizes diameter, h_i defines disk thickness, and ρ_i denotes density. The mass m_i and moment of inertia I_i of the i^{th} particle are, respectively:

$$m_i = \rho_i \frac{\pi D_i^2 h_i}{4} \tag{1}$$

$$I_i = \frac{m_i D_i^2}{8} \tag{2}$$

The i^{th} particle's position, linear and angular velocities progress according to Newton's laws by:

$$\frac{d\mathbf{X}_i(t)}{dt} = \mathbf{V}_i(t) \tag{3}$$

$$m_i \frac{d\mathbf{V}_i(t)}{dt} = \mathbf{F}^T{}_i = m_i \mathbf{g} + \mathbf{F}^d_{i\in k}(t) + \mathbf{F}^c_i(t) \tag{4}$$

$$I_i \frac{d\omega_i(t)}{dt} = \mathbf{T}_i \tag{5}$$

with $\mathbf{F}^T{}_i$ as the net sum of all forces acting on the i^{th} particle, $\mathbf{g}$ as the acceleration due to gravity, $\mathbf{F}^d{}_{i \in k}$ as the total drag force on i^{th} particle residing in k^{th} cell, $\mathbf{F}^c{}_i$ as the net contact force due to contact with other particles or system boundaries, and $\mathbf{T}_i$ as the sum of all torques acting on the i^{th} particle. Because this study does not consider any carrier phase (fluid or gas) we neglect drag forces following the independent tests in the experiments from *Estep and Dufek* [2012] that showed interparticle and body forces are much greater than drag forces caused by the ambient atmosphere as well as wall friction at system boundaries.

Particle contact forces have most often been described by an elastic

spring and a viscous dashpot model in parallel, depicted in Figure 11, whose equation for motion is shown in the normal direction by the following expressions [*Ji and Shen,* 2006; *Malone and Xu,* 2008]:

$$\mathbf{F}^c = \mathbf{F}^e + \mathbf{F}^v \quad (6)$$

$$\mathbf{F}_e = k_n \delta^\alpha \quad (7)$$

$$\mathbf{F}_v = \eta \mathbf{u} \delta^\beta \quad (8)$$

where m is particle mass, δ is overlap between particles (or deformation), η is the damping coefficient, k_n is normal contact stiffness, $\mathbf{F}_e$ is the elastic (spring) force, $\mathbf{F}_v$ is the viscous (dashpot) force, $\mathbf{u}$ is the relative velocity of the two particles moving towards each other, and the values of α and β vary based on the contact model employed. The above denotes the Hertz contact model when α = 3/2, β = 1/4 [*Tsuji et al.,* 1993], which we adopt in this work for two primary reasons: (1) This model has been shown to be a reasonable approximation for granular flows [*Ji and Shen*, 2006; *Brewster et al.,* 2008; *Malone and Xu*, 2008], and (2) We can calculate the contact stiffness for the photoelastic disks a function of deformation using the Herztian contact model from the material's Young's modulus, Poisson ratio, and the disk radius, all properties we can measure independently [*Coste and Giles,* 1999; *Campbell*, 2006; *Brewster et al.,* 2008; *Garg et al*., 2010; *Estep and Dufek*, 2012].

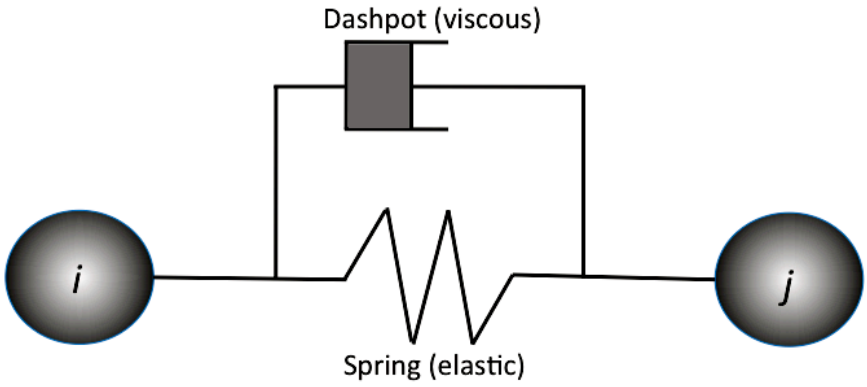

Figure 11. Schematic shows a spring-dashpot soft sphere contact model for two particles, i and j. The spring (elastic) force component is controlled by the contact stiffness parameter *k* in equations 7,9 and 10, while the dashpot (viscous) force component depends on the damping coefficient η in equations 8 and 11.

Using the Hertzian contact theory and assuming a monodisperse grain population, the normal and tangential contact stiffnesses between contacting particles *i* and *j* can be calculated as follows:

$$k_{n,ij} = \frac{2}{3}\frac{E\sqrt{r}}{\left(1-\sigma^2\right)}\delta_{n,ij}^{\frac{1}{2}} \qquad (9)$$

$$k_{t,ij} = \frac{4}{3}\frac{E\sqrt{r}}{\left(2-\sigma\right)\left(\sigma+1\right)}\delta_{n,ij}^{\frac{1}{2}} \qquad (10)$$

with *E* denoting the Young's modulus, *r* corresponding to disk radius, and σ representing the Poisson ratio.

While stiffness constants describe the elastic properties of simulated particles, the dissipative properties depend on the coefficient of restitution, which is simply the ratio of speeds after and before a collision [*Massey et al.,* 2006]. A

relationship between the damping coefficient η and coefficient of restitution e can be found using the following relationship [*Ting et al.,* 1989]:

$$\eta = \frac{2(\ln e)\sqrt{m k_n}}{\sqrt{(\ln e)^2 + \pi^2}} \qquad (11)$$

Values used for the coefficients of restitution for particle-particle and particle-wall contacts originate from experimental trials of free falling particles impacting the designated material while being recorded by a high-speed camera. Particle velocities were calculated by dividing particle displacement by elapsed time for sequential images of the frames surrounding the captured impacts. The coefficients of restitution for particle-particle and particle-wall contacts were measured as 0.355 ± 0.121 and 0.473 ± 0.091, respectively. Error values represent one standard deviation for the cumulative data about the mean.

For validation of the numerical model compared to the experimental data, we ran 222 total simulations using 3 substrate inclinations and 10 values of contact stiffness. We collected simulated data consistent in form with the experimental data. To extract relevant information we first assigned a point in the substrate as a reference position, and searched for active particles within a designated radius of the reference position. Next, forces experienced by the active particle(s) within the designated radius were recorded for the duration of the flow simulation; and exported as a file containing the particle id, time-step, component velocities, and component forces (where component refers to the x- and y-components using an x-y 2D Cartesian coordinate system). The resulting

dataset was filtered such that each particle id – time-step pairing was unique, and force magnitudes were computed for each pairing. From the experiments, the mean peak (force chain) bed force, the time-averaged value of the measured localized bed force magnitudes, was obtained from analyzing the fringe factor of the chain member contacting the substrate. Peak forces in the simulation data were identified and correspond to force chain transmitted near-bed forces.

Flow height bed forces were calculated for the simulated flows with the same method used in the experimental analysis. Time-averaged flow height bed forces were estimated from the height of the flow normal to the force chain-substrate contact point to generate a point of comparison with those forces we would predict from a depth-averaged perspective. Depth-averaged continuum models often calculate normal bed stresses by assuming that vertical stresses are dominated by weight of the flow immediately above the bed. The flow height bed force we report here is used to compare the results to depth-average continuum models as a base line.

Simulations of sand grains and rocks flowing down an incline were also conducted using our discrete element model. The sand and rock flow simulations used the same system configuration as the simulated experiments, and only differed in the physical properties input for the active flow particles. *Cole and Peters* [2008] conducted experiments that provided constraints on the values for sand and rock grain contact stiffnesses and densities, which we use in our simulations. The sand and rock flow simulations were conducted to provide a

comparison between the materials used in previous experiments [*Estep and Dufek*, 2012] and natural materials.

Although previous work showed qualitative agreement between 2D and 3D granular simulation results [*Alonso-Marroquín et al.,* 2009], contributions from 3D structure, as well as polydispersity, irregular terrain, and pore fluids cannot be assumed. While not evaluated in this work, the propagation of force chains into the subsurface below and in front of the flow may modify pore pressures in those substrates that are at or near liquid saturation. Irregular terrain also likely influences force chain evolution and the impact forces these chains impose on substrates; for instance bumpy topography may exacerbate chain forces, resulting in particle fragmentation within the flow body [*Davies and McSaveny*, 2009; *De Blasio,* 2011].

CHAPTER 6. DISCRETE ELEMENT METHOD NUMERICAL RESULTS

Results from the analog experiments of *Estep and Dufek* [2012] are compared to the discrete element simulations results previously described, in consistent forms so that the data are comparable. Further results present numerical performance in a broader context by showing peak forces as a function of the value of contact stiffness. The remaining results explore force probability distributions as a function of contact stiffness, and finally test for characteristic periodicities of peak forces.

Experimental bed-force time series were presented in Figure 6 of Part 1 for each inclination of the rigid bed experiments. The data, a summation of localized (force chain) and flow height bed forces, focus on the bed forces within an approximately 0.012 m length section on the ramp surface over the duration of each flow. These time series show bed forces at one position on the substrate as the flow passes. Time series of bed forces from simulation data are presented in Figures 12, 13, and 14 which correspond to 10, 20, and 30-degree substrate inclinations, respectively. These simulation time series contain information specific to interparticle forces and do not include the flow-height baseline observed in the experimental bed force time series (Figure 6). External file Media 3 shows a simulated monodisperse flow animation.

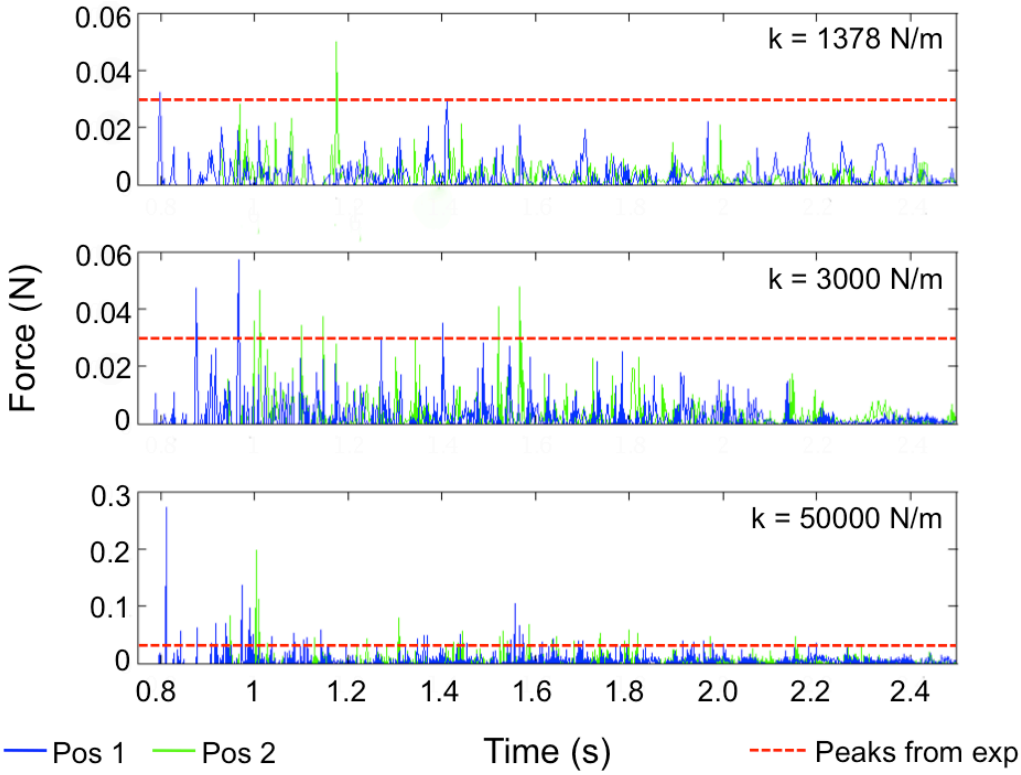

Figure 12. Bed force time series from simulations with a 10-degree ramp inclination. Contact stiffness values (k) of 1378 N/m, 3000 N/m, and 50000 N/m correspond to the top, middle, and bottom times series, respectively. Green solid lines and blue solid lines indicate the location of data collection as Position 1 and Position 2, respectively. Position 1 was 0.1 m down slope of the release gate and Position 2 was 0.2 m down slope of the release gate. The red horizontal dashed lines represent the mean peak forces from the photoelastic experiments with a 10-degree ramp.

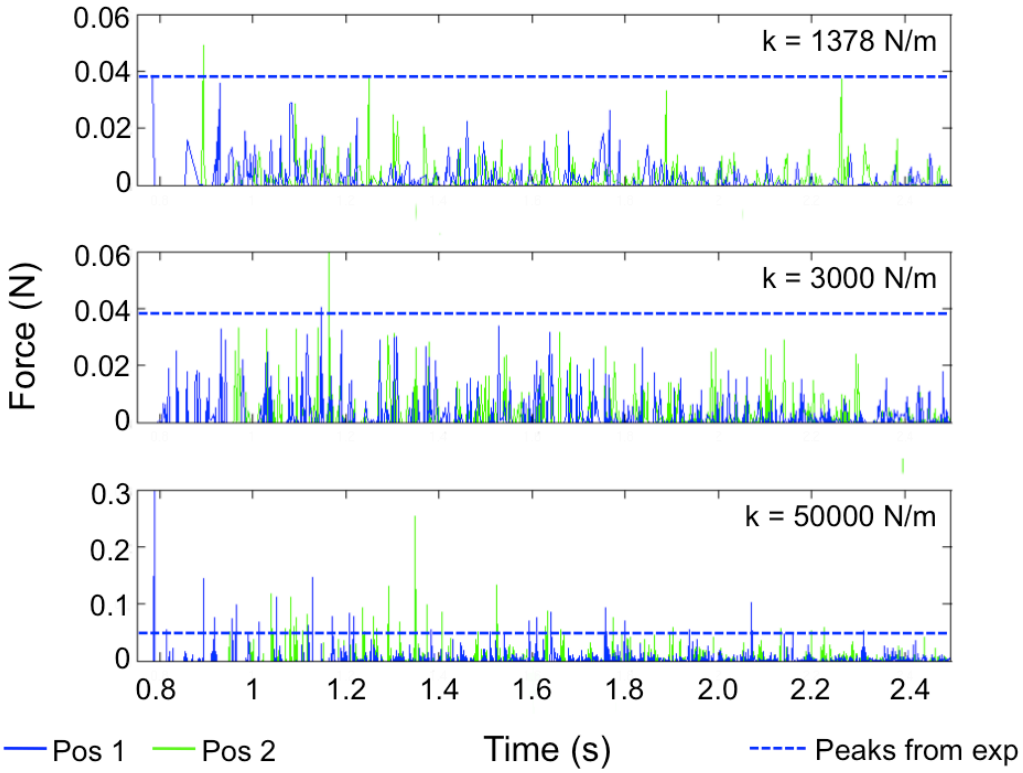

Figure 13. Bed force time series from simulations with a 20-degree ramp inclination. Contact stiffness values (k) of 1378 N/m, 3000 N/m, and 50000 N/m correspond to the top, middle, and bottom times series, respectively. Green solid lines and blue solid lines indicate the location of data collection as Position 1 and Position 2, respectively. Position 1 was 0.1 m down slope of the release gate and Position 2 was 0.2 m down slope of the release gate. The red horizontal dashed lines represent the mean peak forces from the photoelastic experiments with a 20-degree ramp.

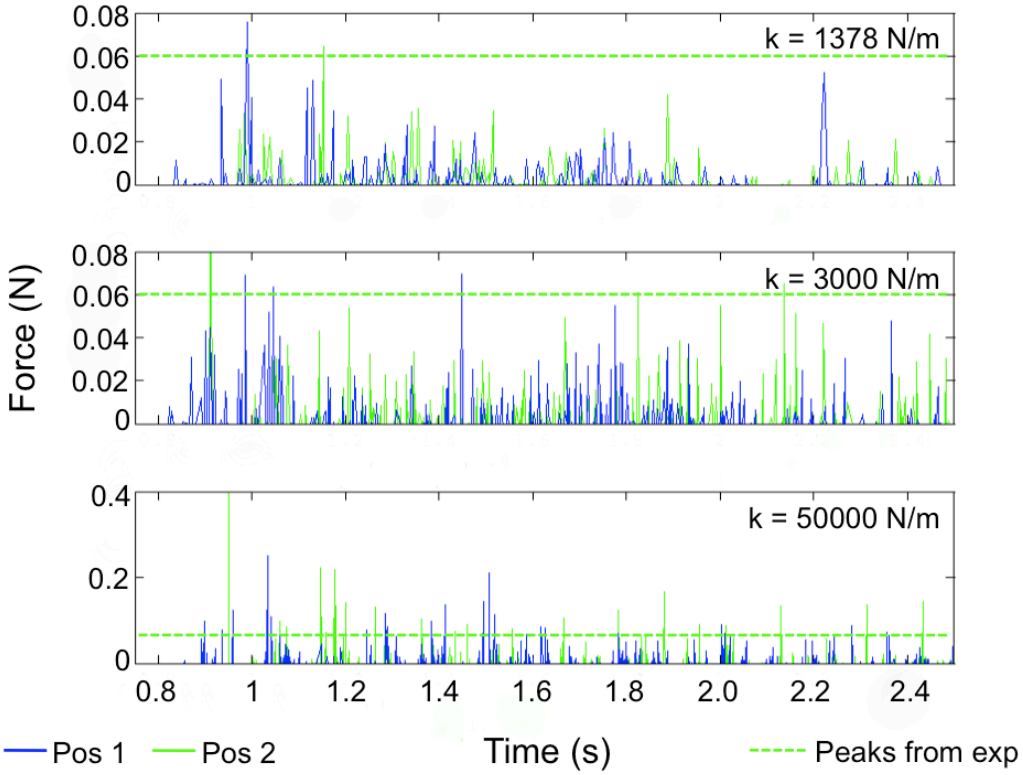

Figure 14. Bed force time series from simulations with a 30-degree ramp inclination. Contact stiffness values (k) of 1378 N/m, 3000 N/m, and 50000 N/m correspond to the top, middle, and bottom times series, respectively. Green solid lines and blue solid lines indicate the location of data collection as Position 1 and Position 2, respectively. Position 1 was 0.1 m down slope of the release gate and Position 2 was 0.2 m down slope of the release gate. The red horizontal dashed lines represent the mean peak forces from the photoelastic experiments with a 30-degree ramp.

Based on the magnitude of particle deformation observed in our experiments we calculated contact stiffness for the experimental disks to fall within a range of approximately 1300 to 2600 N/m. The range of values arises due to variations in measured particle deformation between the end-member fringe magnitudes observed in the experiments. We note that contact stiffness values presented here were calculated from physical measurements and are

independent of the numerical tests. Experimental data revealed that time-averaged peak localized (force chain) bed forces relative to flow height bed forces was 435.62 ± 0.59 % for rigid bed conditions, compared to 396.29 ± 0.58 % from simulation data. Peak (force chain) bed forces from the experiments averaged 0.0413 ± 0.0095 N, while flow height bed forces averaged 0.0104 ± 0.0020 N. Simulation data provide peak (force chain) bed forces averaging 0.0456 ± 0.0083 N, and flow height bed forces averaging 0.0105 ± 0.0036 N. Error values for the bed forces denote the mean absolute deviation.

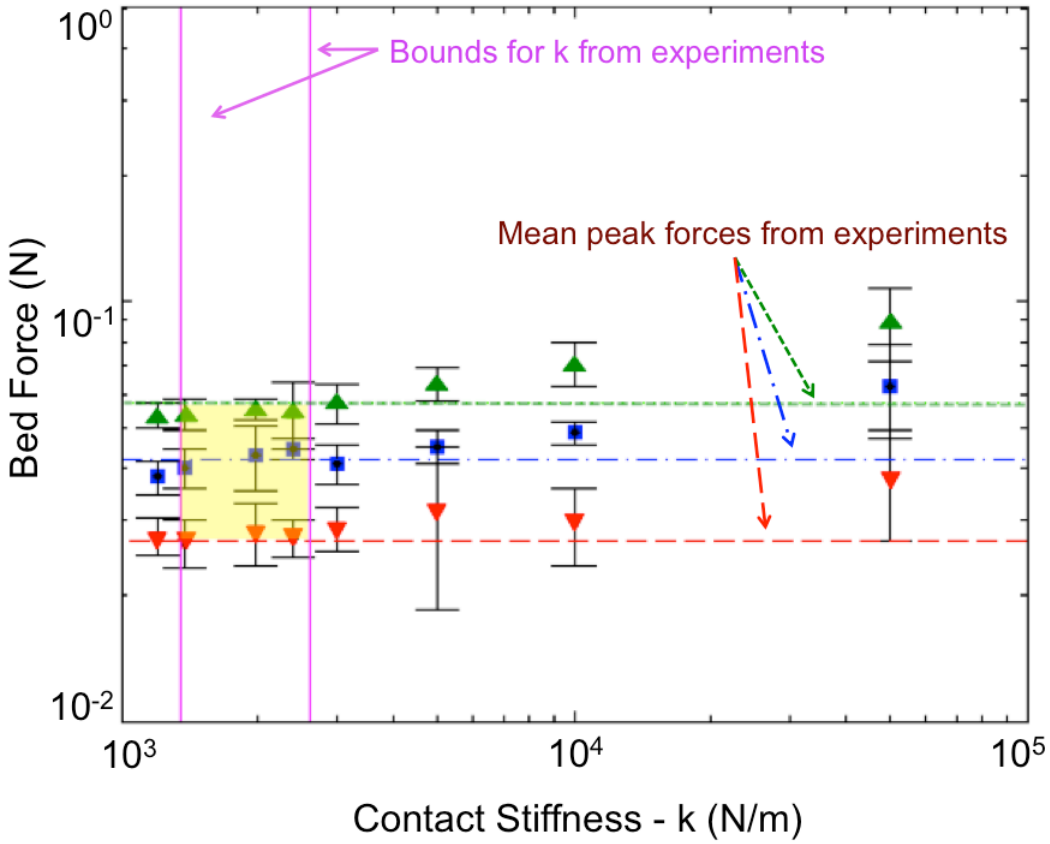

Figure 15. Peak bed force sensitivity to the contact stiffness parameter (k, units N/m) in simulation data. Increases in contact stiffness (k) correspond to increases in peak bed forces for each inclination. The vertical lines indicate the bounds for k values, measured from the experiments. The horizontal red, blue, and green dashed lines represent mean peak forces from 10-degree, 20-degree, and 30-degree experimental data, respectively. Data points represent the simulated mean peak bed forces, and error bars show mean absolute deviation. Red inverted triangles, blue squares, and green triangles represent the 10-degree, 20-degree, and 30-degree cases, respectively. The shaded yellow box covers the area on the plot consistent with experimental data; i.e. simulation data within this box agree with experimental data.

Simulation data show particular sensitivity to the value used for contact stiffness. Figure 15 presents a comparison of peak bed forces to contact stiffness. The ranges for contact stiffnesses and peak bed forces derived from

experimental data is outlined. A ‘validation box’ is created by the overlap of these ranges, such that simulation data within the bounds of this box accurately reproduce the experimental results. We emphasize that the stiffness values bounds for experiments are in fact those determined from physical measurements. Figure 16 shows a probability distribution of bed forces for simulations using contact stiffness values consistent with experimental values. Figure 17 presents a probability distribution of bed forces for simulations using contact stiffness values consistent with experimental values, and adding a contact stiffness value higher than the measured values by a factor of ~2 (k = 5000 N/m). Figure 18 reveals a probability distribution of bed forces for simulations using contact stiffness values consistent with experimental values, and adding a contact stiffness value higher than the measured values by more than an order of magnitude (k = 50000 N/m). Figures 16, 17, and 18 show that increases in contact stiffness correspond to increases in peak bed forces; and that larger excursions are less probable than smaller ones.

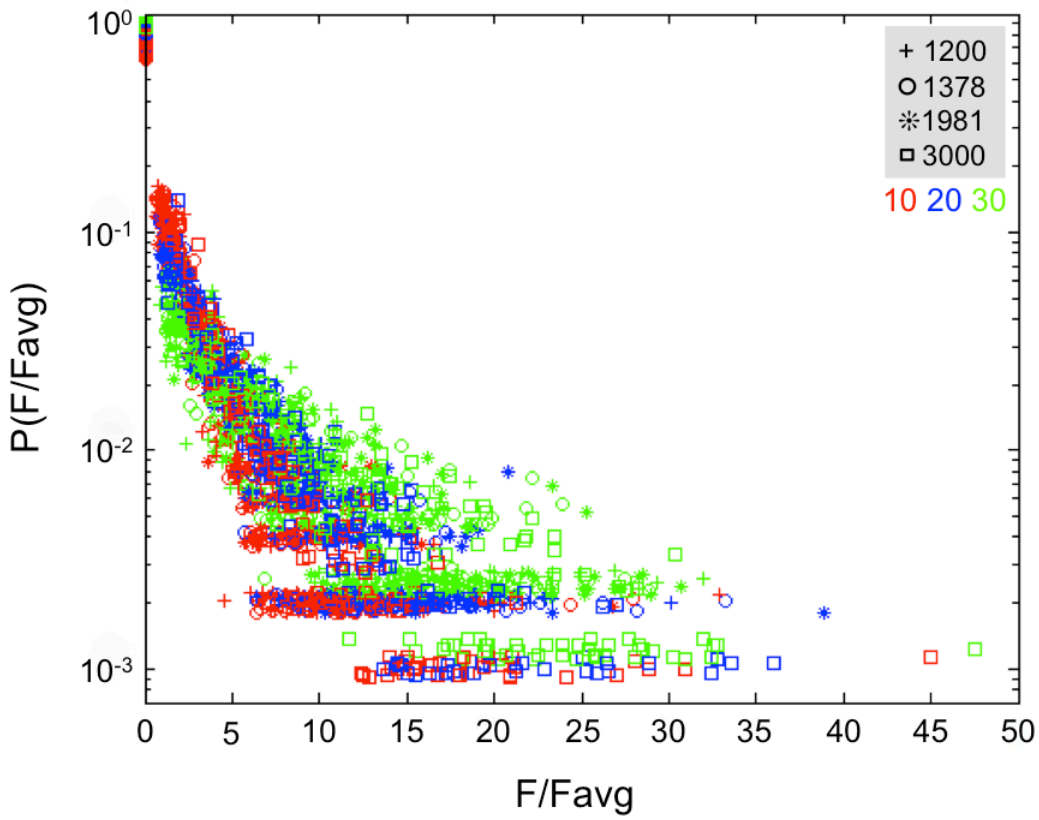

Figure 16. Probability distribution of peak bed forces using contact stiffness values consistent with experimental values. The vertical axis represents probability and the horizontal axis indicates peak bed forces normalized by the mean bed force. Red symbols, blue symbols, and green symbols represent 10-degree, 20-degree, and 30-degree data, respectively. The legend in the shaded box refers to contact stiffness (N/m), while the red, blue, and green colored numbers directly below the shaded box indicate data from 10-degree, 20-degree, and 30-degree data, respectively.

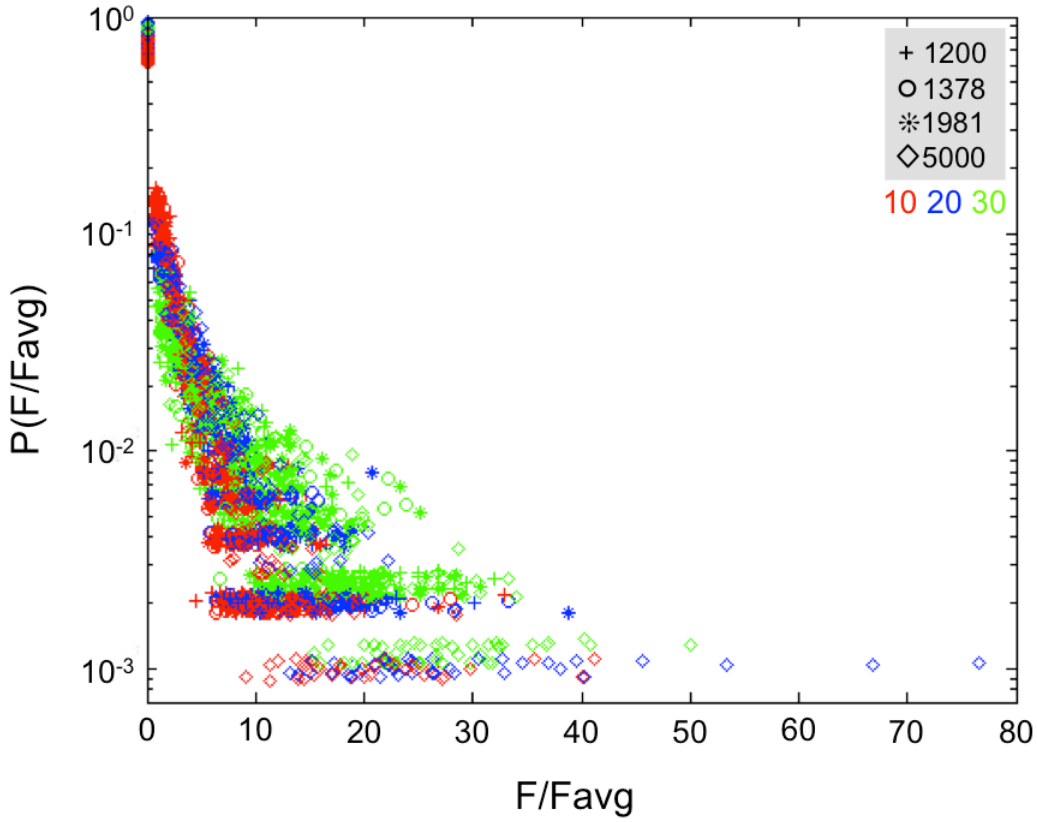

Figure 17. Probability distribution of peak bed forces using contact stiffness values exceeding the experimental range by a factor of 2. The vertical axis represents probability and the horizontal axis indicates peak bed forces normalized by the mean bed force. Red symbols, blue symbols, and green symbols represent 10-degree, 20-degree, and 30-degree data, respectively. The legend in the shaded box refers to contact stiffness (N/m), while the red, blue, and green colored numbers directly below the shaded box indicate data from 10-degree, 20-degree, and 30-degree data, respectively.

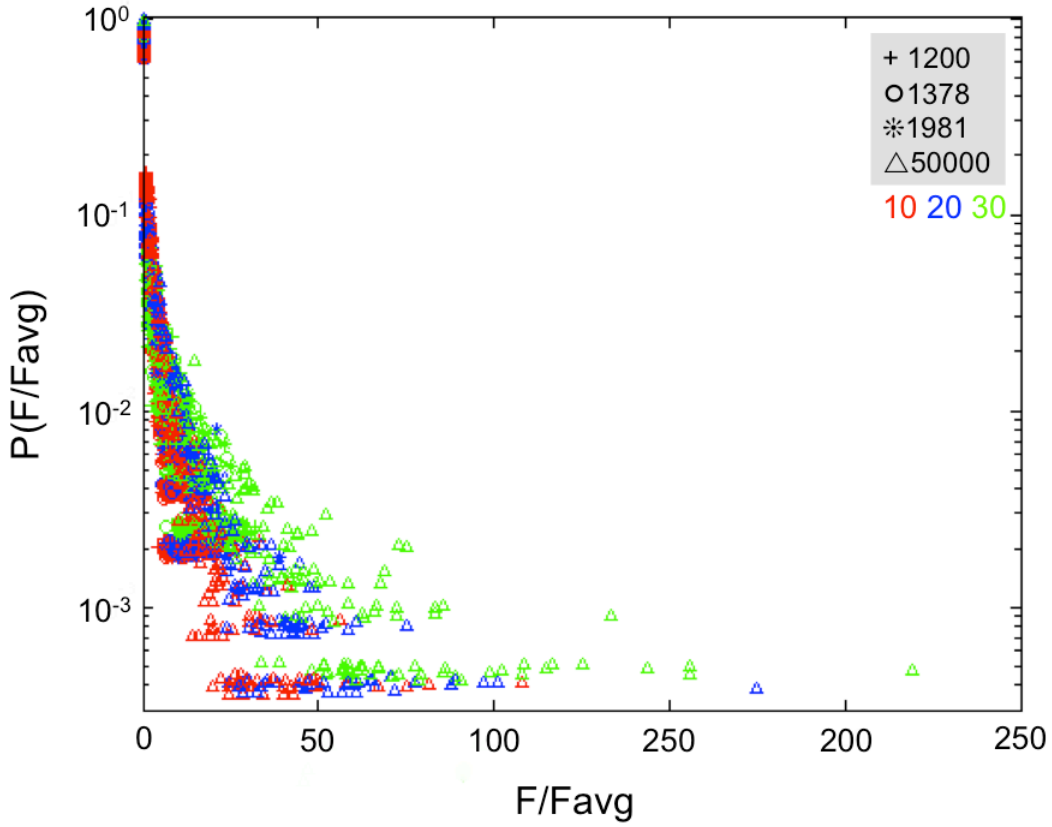

Figure 18. Probability distribution of peak bed forces from simulation data using contact stiffness values exceeding the experimental range by an order of magnitude. The vertical axis represents probability and the horizontal axis indicates peak bed forces normalized by the mean bed force. Red symbols, blue symbols, and green symbols represent 10-degree, 20-degree, and 30-degree data, respectively. The legend in the shaded box refers to contact stiffness (N/m), while the red, blue, and green colored numbers directly below the shaded box indicate data from 10-degree, 20-degree, and 30-degree data, respectively.

Discrete element simulations of 2D sand grain and rock granular flows show bed force data in qualitative agreement with simulated experiments, but with more extreme localization magnitudes (Figure 19). Normalized by the force of a single particles gravitational acceleration ($F_{bed}/F_{particle}$), simulated flow bed forces reached 876 and 686 for sand and rock flows, respectively, compared to

67 for experimental flows. Each of the (sand, rock, and experimental) simulated flows reached and maintained flow heights of roughly 10 particle diameters. Different physical parameters input in the model for sand and experimental particles were contact stiffness, particle diameter, and particle density, which are listed in Table 3. Spectral analysis of bed force time series data generated a noisy amplitude spectrum (Figure 20) that revealed no dominant frequencies.

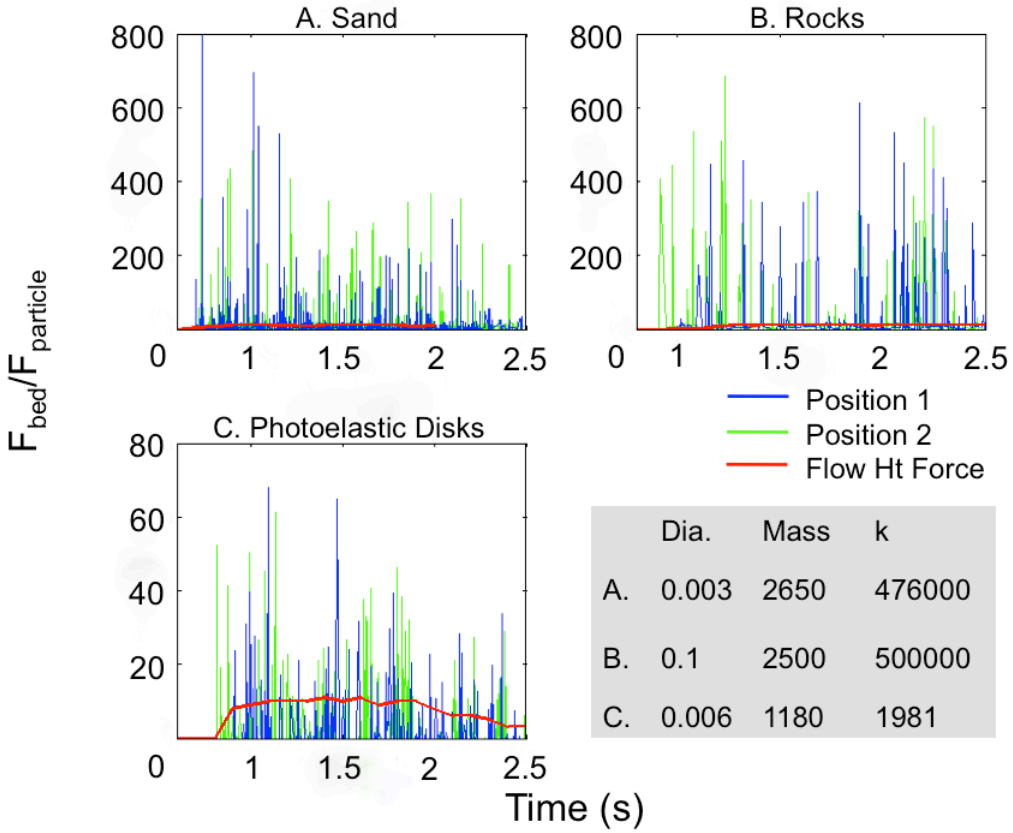

Figure 19. Bed force time series from simulated flows comparing results for natural material properties to experimental material properties. (A) sand grains, (B) rocks, and (C) photoelastic disks from experiments. 'Position 1' and 'Position 2' indicate locations on the substrate down-slope of the release gate where bed force data was collected. 'Flow Ht Force' refers to the expected bed force magnitude calculated from the height of the flow surface above the substrate. The y-axes (bed forces) are normalized by the gravitational acceleration of a single particle. The shaded box shows the values of particle diameter (Dia.) in

meters, mass in kilograms per cubic meter, and contact stiffness (k) in Newtons per meter used for each material.

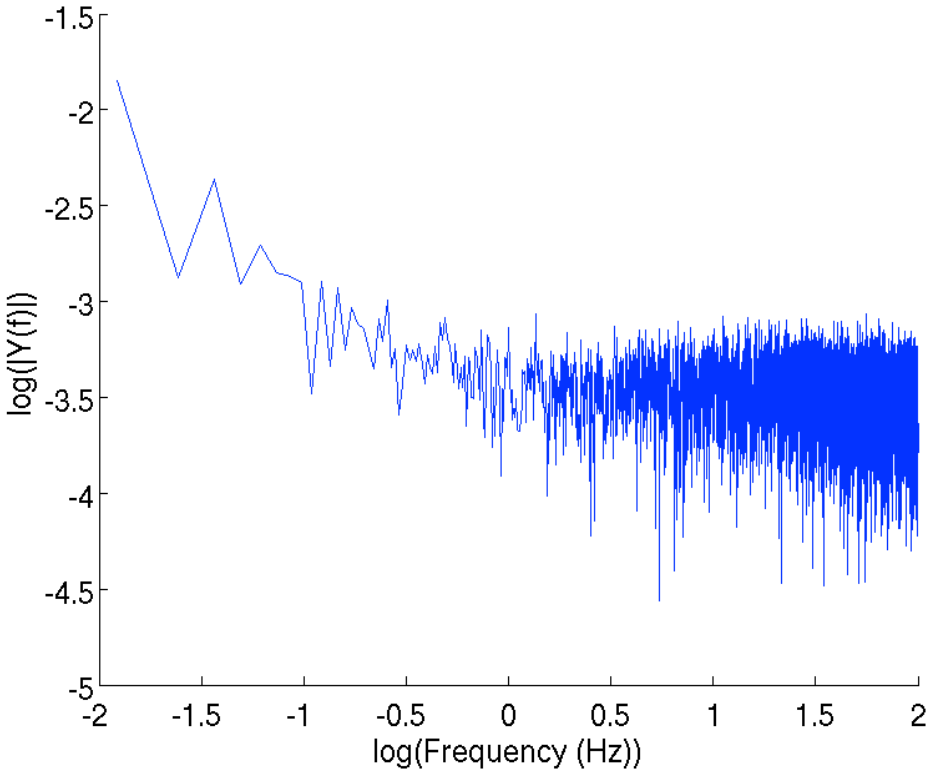

Figure 20. Amplitude spectrum of bed force time series data from a prolonged (30 sec) simulation of 20-degree incline granular flow. The physical properties of the experimental material were used for the particles in the simulation. The spectrum is displayed using a log-log scale with amplitude on the vertical axis and frequency on the horizontal axis. This spectrum shows noise and reveals no characteristic frequencies.

Table 4. Physical parameters used for sand grain and experimental simulations[a]

Material	**d** (m)	**ρ** (kg m^{-3})	**k** (N/m)	$\mathbf{F_{particle}}$ (N)
Sand	0.003	2650	476000	0.000275
Rock	0.1	2500	500000	0.2408
Plastic	0.006	1180	1981	0.001040

[a]The variables listed represent a particle's: diameter (d), density (ρ), contact stiffness (k), and gravitational acceleration ($F_{particle}$).

CHAPTER 7. DISCRETE ELEMENT MODEL SIMULATIONS DISCUSSION

Results from our numerical simulations show strong agreement with the data from the experiments in *Estep and Dufek* [2012], which provides a reasonable validation to our DEM model. Our data show that discrete element simulations accurately reproduce the bed force excursions due to force chains that have been observed experimentally. The results imply that continuum models utilizing depth-averaging schemes for bed forces may transiently under-predict the force chain transmitted localized bed forces. Further, because particles contacting the substrate are often spectators (they bear no significant load in the granular system), our work implies that the depth-averaged approach may also transiently over-predict bed forces as well. The significance of the bed force deviations observed relative to entrainment processes is unclear from our results. The short durations of the force chain transmitted bed forces may impede entrainment ability. Although previous studies have shown that contact timescales in dense shearing flows are not limiting to long-range force transmission [*Sun et al*., 2010; *Estep and Dufek*, 2012], further work is necessary to determine if the transmitted bed forces are legitimate entrainment mechanisms on natural spatial and temporal scales. Spectral analysis of a 30 second duration flow suggests that no characteristic frequencies are present in the resulting bed force time series data. This limited frequency analysis implies that the fluctuating bed forces imposed by force chain activity likely will not induce oscillatory motion

on bed particles that may enhance entrainment susceptibility (analogous to rocking a vehicle stuck in the mud to mobilize it). However, subsequent feedback between erosion, bed roughness evolution, and force chain evolution is not considered with the static bed used here.

Data show that simulation results are most sensitive to the contact stiffness input parameter. Increases in contact stiffness caused corresponding increases in peak bed forces universally. Linearity in the log-log plot of contact stiffness vs. peak bed forces suggests an exponential relationship, however this assertion is preliminary without a larger dataset. Numerical and experimental data agree strongly when using contact stiffness values in the range calculated from measured particle deformations in experiments and using the Hertzian contact model [*Tsuji et al.,* 1993; *Garg et al.,* 2010]. We note that stiffness values were not tuned to get good correspondence with experiments, rather the stiffness values that give the best correspondence with experiments are those who have realistic properties determined from independent physical measurements. These results further support validity of the Hertzian model for discrete element simulations, and suggest a higher degree of bed force localization due to force chains in natural flows (because natural materials, such as rock or sand, have much higher contact stiffness values). Simulations using physical properties of sand and rock indeed show more extreme bed force localization relative to simulations using the properties of soft plastic disks.

Because previous studies have generated two opposing conclusions, the influence of contact stiffness values on the physical behavior of dynamic granular systems has been indeterminate. *Campbell* [2006] postulated that particle stiffness governs how particles 'see' each other mechanically and thus determines bulk elastic properties of granular materials. *Sun et al.* [2010] followed the sentiment of *Campbell* [2006], but added that stiffness determines the strength and stability of force chains. Further endorsement that contact stiffness significantly influences granular behavior was shown in *Ji and Shen* [2006], *Moreno-Atanasio et al.* [2007]*, Aranson et al.* [2008], and *Brewster et al.* [2008]. Conversely, some studies have reported that changing the value of contact stiffness did not significantly alter physical dynamics of granular systems [*Yuu et al.,* 1995; *Milburn et al.,* 2005; *Rycroft et al.,* 2009]. As the results of the current work show, we observe a distinct quantitative sensitivity on grain-scale behavior resulting from variations in the contact stiffness value. Additionally, qualitative macro-scale behavior modifications were observed due to variations in contact stiffness in our work. In the simulations, increases in the contact stiffness values coincided with more rigorous bouncing of particles at or near the surface of the granular assembly during delivery into the gated domain and also during the flow after the gate was raised. These quantitative and qualitative results imply that constraining appropriate values for contact stiffness in DEM simulations of natural systems is important for generating accurate physical behavior. The timescale exercise presented in *Estep and Dufek* [2012] further suggests that the

formation of long chains may be more likely in systems consisting of particles with high contact stiffnesses compared to low stiffness particles. This implication comes from the positive correlation of contact stiffness and magnitude difference between force propagation- and contact- time scales (i.e. for sand particles and photoelastic disks the force propagation timescale is ~10^{-5} s and ~10^{-4} s, respectively; compared to contact timescales ~10^{-2} s for each case).

Our simulations of a sand and rock flows indicate that the fluctuating bed forces observed experimentally with soft plastic particles also occur with very stiff particles. These results further support the assertion that long-range force propagation is probable in naturally occurring dense granular flows, including those generated during dense volcanic flows. An interesting and obvious characteristic of the sand and rock flow simulation data is that the localized bed force magnitudes are much higher when compared to the experimental simulations. Because the system geometry and relative flow heights for each of the systems is consistent, the differences in contact stiffness and material density must explain the contrasting results observed in Figure 11.

7.1 Discrete Element Method Simulations Conclusion

While simplified, the current work provides compelling evidence that bed force localizations due to force chains exist and suggests that these forces may

be important for entrainment of substrates during dense volcanic granular flows due to the magnitude of the excursions. Our results indicate that accurate prescription of values for contact stiffness in DEM granular flow simulations is very important in order to produce accurate bed conditions. This work also demonstrates that the discrete element approach is particularly useful for granular flows, because although force chains operate as mesoscale structures in length, they terminate (and thus transfer forces) at the particle scale. Although the contributions of 3-dimensional structure, polydispersity, fluids, and irregular terrain are untested here, these simulations provide a general foundation for continuing work towards implementation of more complicated system components.

PART 3. CONTINUED WORK

CHAPTER 8. BIDISPERSE GRANULAR POPULATIONS

The methodology described in Parts 1 & 2 was implemented for granular systems composed of bidisperse populations. These analog and numerical experiments were designed to observe bed force behavior in systems composed of the bidisperse grain size ratio range of 1:1, 2:1, and 4:1 (each ratio denotes the number of small:large disks). Minor modifications to the physical laboratory apparatus and analog methods, detailed in the next section, were required to accommodate bidisperse analysis. Changes in the geometric properties of the analog apparatus and initial conditions for each bidisperse system, the only necessary changes to the computational model, were replicated in the numerical simulations. Results from bidisperse experiments resemble monodisperse analyses, and confirm that force chains cause significant bed force localization in mixed grain size populations.

Chapter 8.1 Bidisperse Analog Experimental Modifications

The photoelastic apparatus for bidisperse experiments was essentially the same as the one used in the monodisperse investigation, except that the ramp incline was held at a constant angle of 32.5 degrees. An additional chamber was attached to the bottom of the apparatus, which facilitated the segregation of disks

by size. Flow particles fell into the added chamber after traversing the study area, so that the addition had no influence on flow properties. The added segregation chamber provided a way to initiate sequential runs consistently by allowing replicate introduction of the two disk sizes back into the apparatus. A Maxant Techline (STS21NFMX) X-ray illuminator was acquired for the bidisperse runs, resulting in a more consistent and brighter light source that enabled an increase to 600 frames per second for recording (compared to 200 fps for monodisperse runs).

Bidisperse populations with [small:large] size distributions of [1:1], [2:1], and [4:1] were used in the runs, in addition to a monodisperse system for control. A total of 16 experiments were conducted, 5 for each bidisperse system and 1 for the monodisperse system. Table 5 shows the disk counts used for each size ratio employed in the experiments, and the total body force for each bidisperse system. The absolute numbers of small and large disks were chosen on the basis of equitable hopper occupation between population size ratios (i.e. each population takes up approximately the same area prior to gate release). Vishay Precision Group's PSM-4 Photostress photoelastic material, as in the monodisperse experiments, was used to fabricate 0.012 m diameter disks for the new mixed population runs.

Table 5. Bidisperse disk populations, flow body force, and number of runs

Size ratio *(Small:Large)*	**Small Disks** *(0.006 m)*	**Large Disks** *(0.012 m)*	**Flow Body Force** *(N)*	**# of Runs**
Mono	896	0	0.8614	1
1:1	240	240	0.9686	5
2:1	360	180	0.8995	5
4:1	512	128	0.8858	5

Chapter 8.2 Bidisperse Analog Experimental results

Analog photoelastic experiments using bidisperse granular systems exhibit bed force data consistent with the results in Part 1 both qualitatively and quantitatively. Bed force time series in Figure 21 show results for each mixed population as well as the monodisperse control system. Peak bed force magnitudes, normalized by expected bed forces due to flow height, increase for mixed populations relative to the monodisperse system. The peaks for mixed systems also appear to occur at a higher frequency, although this behavior is yet to be quantified. Comparisons of mean peak forces and maximum peak forces are displayed in Figure 22, which further illustrate that mixed population systems trend to larger peak bed forces relative to monodisperse systems. External files

Media 4 and Media 5 show an analog bidisperse experiment video clip and collage of analog bidisperse experiment force chain images, respectively.

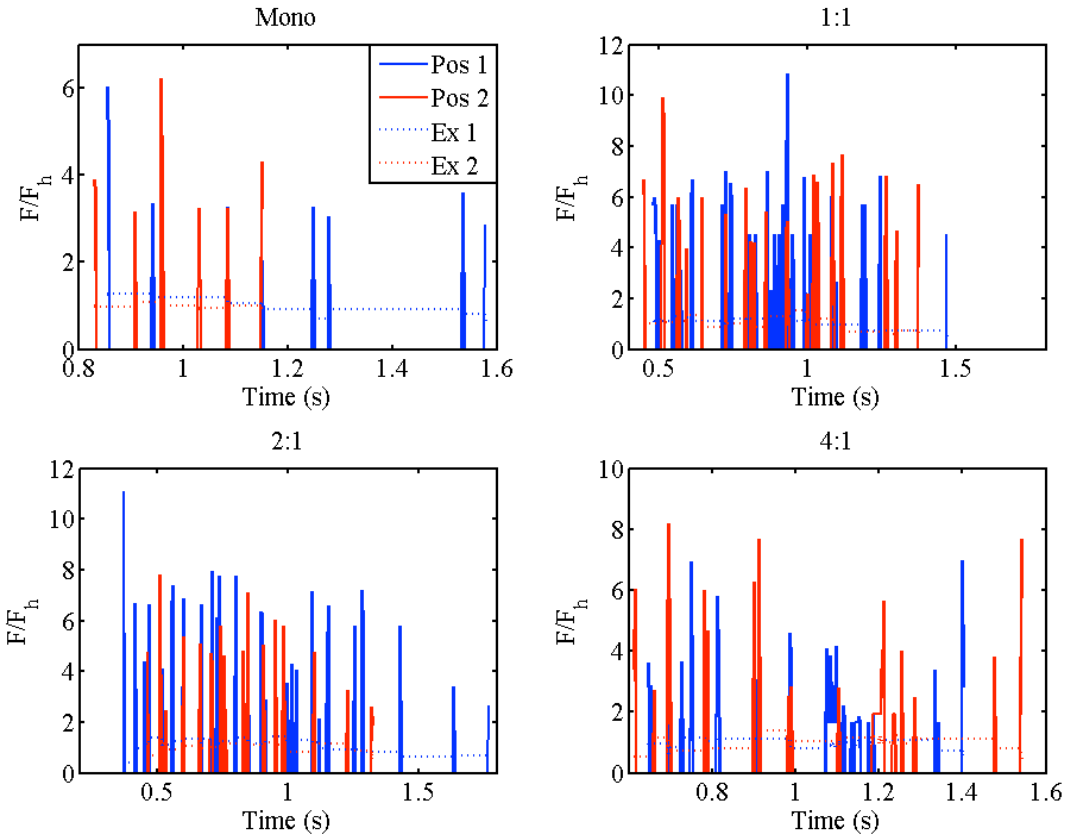

Figure 21. Bed force time series from bidisperse analog experiments show behavior consistent with monodisperse results. The y-axes are peak bed forces F (due to force chains) normalized by mean depth-averaged bed force Fh (expected due to flow height). Pos 1 and Pos 2; colored blue and red, respectively, indicate the recording positions located on the ramp down slope of the release gate, and Ex 1 and Ex 2 correspond to the expected bed force due to flow height. The panels distinguish between grain size distributions: mono – monodisperse, 1:1 – equal number of small and large disks, 2:1 – 2x small disks compared to large, 4:1 4x small disks compared to large.

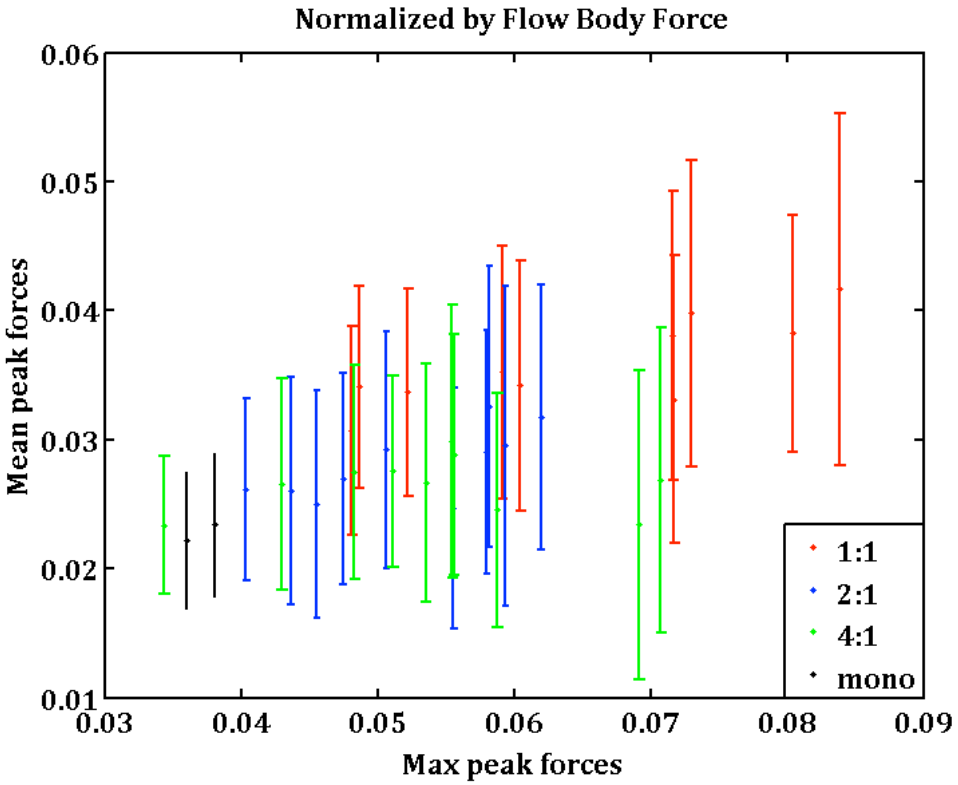

Figure 22. Comparisons of analog bidisperse peak bed forces, which are normalized by total flow body force, between (small:large) population ratios 1:1 (red), 2:1 (blue), and 4:1 (green) with monodisperse (black) systems show similar behavior for all populations. Error bars represent one standard deviation about the mean value. Flow Body Force for each system is listed in Table 5.

Chapter 8.3 Bidisperse Numerical Experimental Modifications

The MFIX DEM code detailed in Part 2 was also utilized for the bidisperse simulations, which replicated the analog bidisperse experiments discussed above. Modifications to the particle generator subroutines were necessary to implement the mixed populations shown in Table 5. Adjustments were also made to the fixed ramp and release gate generator files to accommodate the 32.5-degree inclination. Beyond the geometric adaptations above, the settings and

parameters used in previous simulations remained in place. The physical properties of, and contact model for particle-particle and particle-wall interactions are assumed appropriate for both large and small disks because they consist of the same material. To date, one simulation for each mixed and monodisperse system has been completed, and results are shown below.

Chapter 8.4 Bidisperse Numerical Experimental Results

Numerical experiments using bidisperse granular systems exhibit bed force data consistent with the analog experimental results both qualitatively and quantitatively. Bed force time series in Figure 23 show results for each mixed population as well as the monodisperse control system. Peak bed force magnitudes, normalized by expected bed forces due to flow height, increase for mixed populations relative to the monodisperse system. The peaks for monodisperse systems appear to occur at a higher frequency in these simulations, which is converse to the analog results, although this behavior is yet to be quantified. Comparisons of mean peak forces and maximum peak forces are displayed in Figure 24, which illustrate that simulated mixed and monodisperse population systems have similar peak bed forces. A bidisperse numerical simulation animation is shown the external file Media 6.

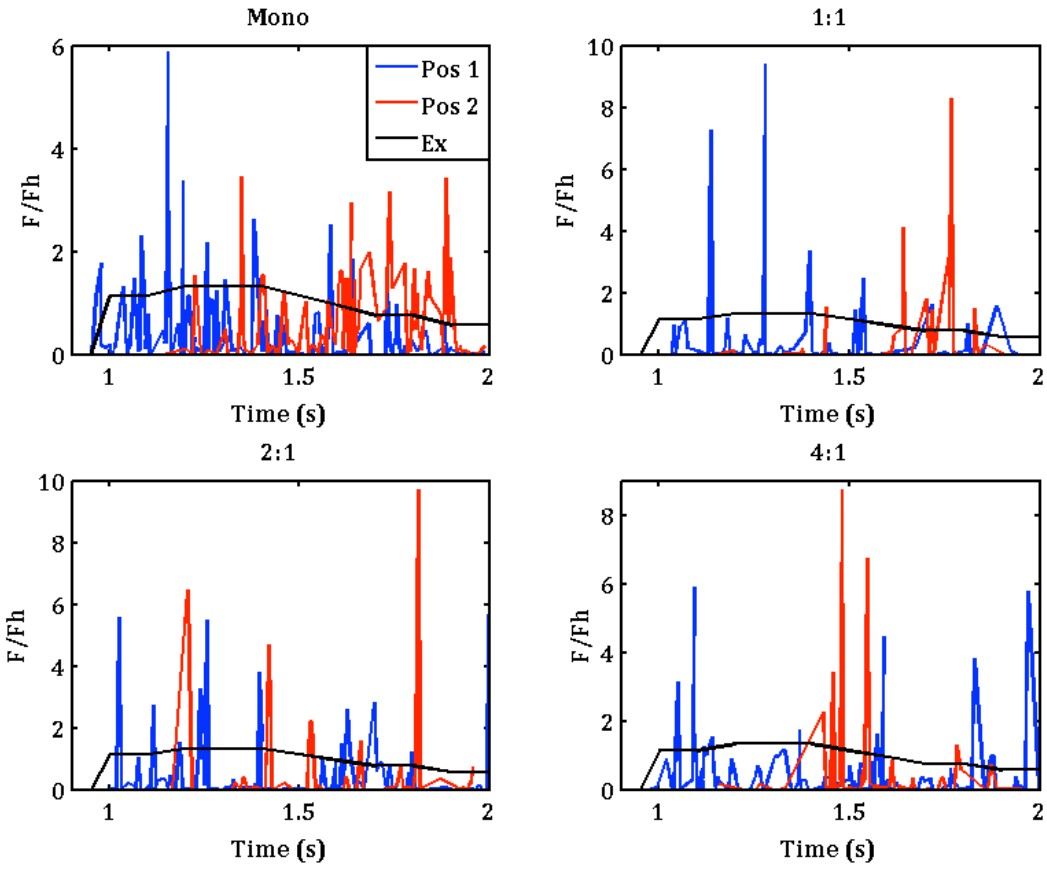

Figure 23. Bed force time series from bidisperse numerical experiments show behavior consistent with analog results. The y-axes are peak bed forces F (due to force chains) normalized by mean depth-averaged bed force Fh (expected due to flow height). Pos 1 and Pos 2; colored blue and red, respectively, indicate the recording positions located on the ramp down slope of the release gate, and Ex corresponds to the expected bed force due to flow height at Pos 1. The panels distinguish between grain size distributions: mono – monodisperse, 1:1 – equal number of small and large disks, 2:1 – 2x small disks compared to large, 4:1 4x small disks compared to large.

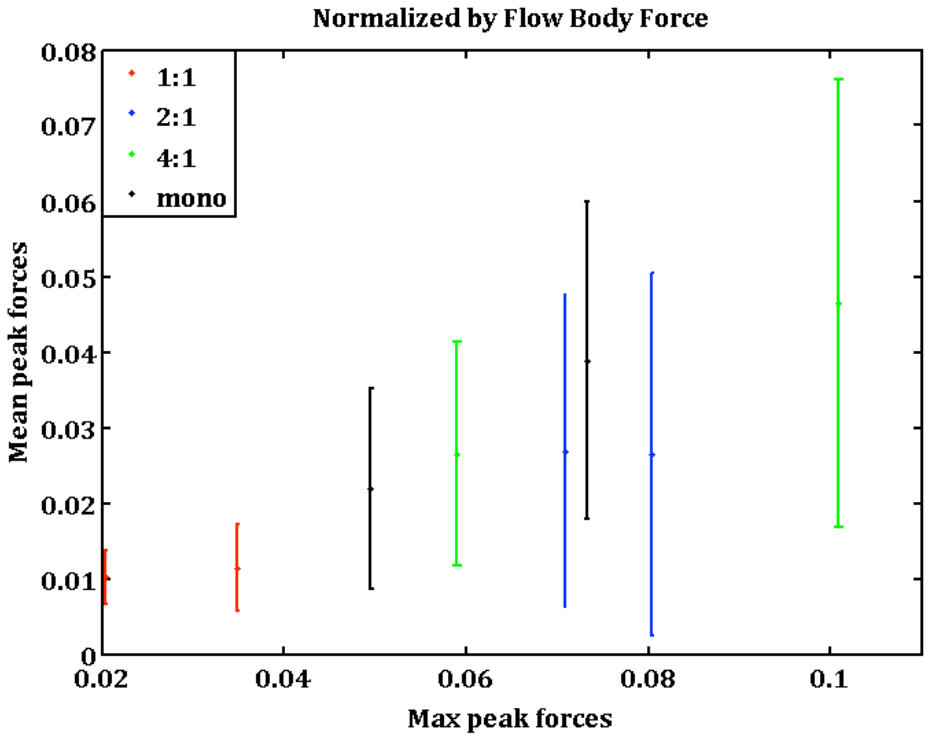

Figure 24. Comparisons of numerical bidisperse peak bed forces, which are normalized by total flow body force, between (small:large) population ratios 1:1 (red), 2:1 (blue), and 4:1 (green) with monodisperse (black) systems show similar behavior for all populations. Error bars represent one standard deviation about the mean value. Flow Body Force for each system is listed in Table 5.

A corollary of this work, that force chains generate significant bed force excursions relative to the depth-averaged approximation, is well illustrated in Figure 25. For each of the mixed and monodisperse systems, peak forces reside well above the unity line for both analog and numerical experiments. The depth-averaged bed forces shown in Figure 25 are derived solely from the flow height, which in these cases are the mean flow height for each respective flow. As compared to Figure 7, the bidisperse results show the same form as previous monodisperse analog results, with a slight increase in the peak values.

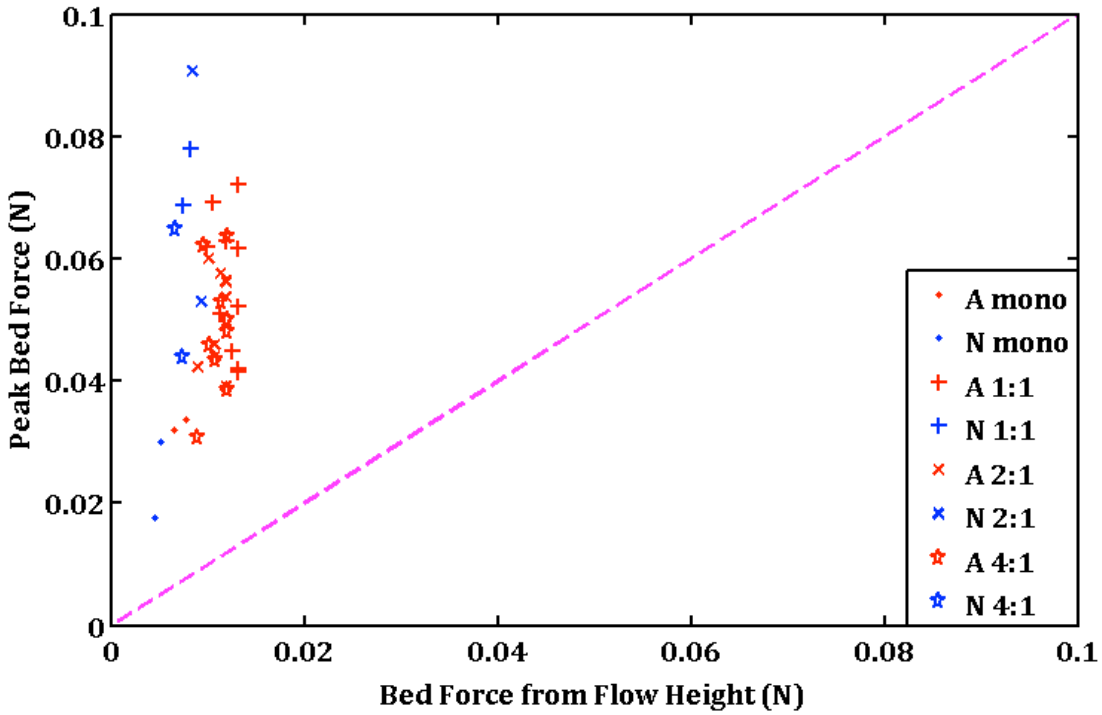

Figure 25. The relationship between peak bed forces and expected bed forces in bidisperse flows follows that observed for monodisperse flows, for both analog and numerical experiments. Marker styles distinguish between grain size distributions mono – monodisperse, 1:1 – equal number of large and small disks, 2:1 – 2x small disks compared to large, 4:1 4x small disks compared to large. 'A' (red) markers represent analog results, while 'N' (blue) markers denote numerical results.

Chapter 8.5 Bidisperse Experiments Discussion

Analog and numerical results for bidisperse systems exhibit consistent behavior in quantitative and qualitative perspectives. Additionally, the bed force characteristics discovered for monodisperse systems from earlier work translate directly into mixed systems. Some obvious differences between the monodisperse and bidisperse bed force behavior are visible, however, such as

increased peak forces in mixed systems and variable apparent peak frequencies across disk size distributions. Also the analog and numerical results, while similar, exhibit relatively shifted bed force magnitudes (slightly higher for analog on average). A potential explanation for the increased peak forces for bidisperse systems stems from the argument that the more complicated arrangements in mixed particle size systems permit more neighbors for any given grain. A result of increased neighbors may be increased communication (read: force transmission) via more convoluted force chains with extensive branching, relative to more straightforward networks occurring in monodisperse systems.

A further potential contribution to these discrepancies lies in the difference in data collection for each experiment type. Analog data only exists for disks that 'light up' due to the birefringence induced by force chains. Conversely, numerical data exists for all flow particles within the defined radius of coverage about the substrate recording location. In essence, the analog peak data has a threshold filter via force chains while the numerical data does not. We could manually set a threshold on the numerical data to account for this and oblige better agreement, however this phenomena leads to a point mentioned in Chapter 7 – that depth-averaged approaches also transiently over-predict observed bed forces.

Basically, we have shown that force chains generate bed forces that far exceed those expected from a continuum approach, even for mixed population granular systems. This work also suggests that, in the case of spectator particles at flow substrates, a continuum approach will also overestimate bed forces locally

on grain scales. So the real world picture for bed forces at granular flow substrates is wildly fluctuating bed forces that range from zero to order(s) above the 'expected.' Still missing from this analysis are interstitial fluids and the 3rd dimension, which are commented on below. The final chapter (11) postulates about a constitutive relationship for treating this fluctuating behavior of granular flow bed forces.

CHAPTER 9. INTERSTITIAL FLUIDS IN GRANULAR ASSEMBLY

We conducted analog experiments to investigate how interstitial fluids influence the development of force chains and the transmission of long-range forces to saturated flow substrates via force chains. Unfortunately, these endeavors proved fruitless. A density difference of only 5.9% between the fluid (water; 1000 kg/m^3) and solid (photoelastic disks; 1061.5 kg/m^3) proved too small for the system to achieve adequate interparticle forces to generate birefringence. Sufficient room and materials to construct an apparatus/system large enough to successfully produce birefringence in water-saturated conditions eludes us. Intuitively, one can speculate that pore pressures will reduce interparticle forces in a saturated granular system as in Terzaghi's relationship for effective stress in soil mechanics [*Santamarina et al.,* 2001]:

$$\sigma' = \sigma - u \qquad (12)$$

where σ' is effective stress, σ is total stress, and u is pore fluid pressure. This simple relationship assumes hydrostatic fluid pressure and a static solid skeleton, so applicability to dynamic granular systems with non-hydrostatic fluid pressures is questionable and of interest. This problem may be explored in further detail computationally, as a part of future work.

CHAPTER 10. THREE DIMENSIONAL NUMERICAL EXPERIMENTS

The photoelastic technique used in this work is fundamentally restricted to 2-dimensional analysis. Expansion of the force chain bed physics analysis into 3-dimensions is of great interest, and is a process that must be approached computationally. The strong agreement exhibited between the analog and DEM numerical results detailed earlier suggests that our model is robust in terms of capturing the dynamics involved in force transmissions that cause bed forces to vigorously fluctuate. A probability distribution for a 3D simulation of a 4000 particle 4:1 (small:large) bidisperse flow moving down a 3 meter x 0.1 meter ramp plane inclined at 31 degrees is shown in Figure 26. These data are un-scaled, however they are encouraging and demonstrate a large dynamic range for bed forces in a simple, small 3D granular flow. Note that the mean recorded bed force for these data is 5.74e-4 N, the maximum-recorded bed force peak is 1.26 N, and the maximum (initial) depth-averaged bed force for this flow is 0.26 N. This information suggests the behavior established in our 2D experiments translates into 3 dimensions. The external file Media 7 shows an animation of the bed force evolution throughout the duration of flow motion as a series of transient spikes superimposed on the flow substrate plane. Clearly depicted are several localized bed forces with varied magnitudes, which qualitatively follow the behavior observed during previous work. These results show promise for the

further relaxation of system constraints, which steers in the direction of more realistic events.

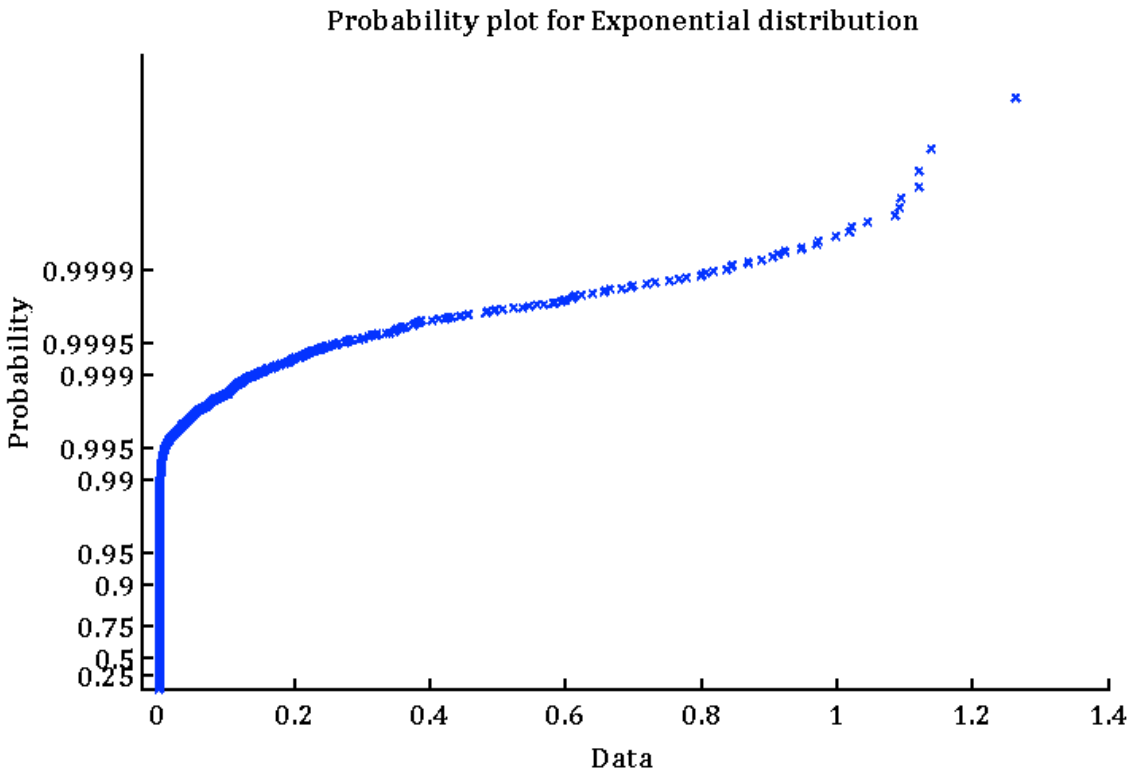

Figure 26. Probability plotted on the y-axis for un-scaled 3D bed force data (in N; x-axis) from a 4000 particle, 4:1 (small:large) bidisperse flow moving down a 3 meter x 0.1 meter ramp plane inclined at 31 degrees. The mean bed force for these data is 5.74e-4 N, the maximum bed force peak is 1.26 N, and the maximum (initial) depth-averaged bed force for this flow is 0.26 N.

CHAPTER 11. FUTURE DIRECTION

This work has been quite successful in evaluating force chain contributions through analog and discrete element numerical investigations, however an evident task remains in the pursuit of a constitutive relationship to resolve these processes in continuum computational models. A statistical approach is likely most appropriate for this venture, centered on spatial and temporal probability functions for force magnitudes and frequencies, respectively. For instance, such probability functions may be used with Monte Carlo methods to replace the vertical stress term in the momentum equation of *Denlinger and Iverson* (2004):

$$\tau_{zz}(b) = \rho h(g + d\overline{w}/dt) \qquad (13)$$

where $\tau_{zz}(b)$ is vertical stress at the flow base, ρ is flow density, h is flow height, g is acceleration due to gravity, and dw/dt is depth averaged vertical acceleration. The detailed form and function of how this approach can be implemented is a case for future work.

REFERENCES

Aharonov, E., Sparks, D. (2004), Stick-slip motion in simulated granular layers, *Journal of Geophysical Research, 109(B09216),* doi:10.1029/2003JB002597

Alonso-Marroquín, F., Galindo-Torres, S., Tordesillas, A. and Wang, Y. (2009). New perspectives for discrete element modeling: Merging computational geometry and molecular dynamics. AIP Conf. Proc., 1145: 4.

Ancey, C., Davison, A., and Bohm, T. (2008), Entrainment and motion of coarse particles in a shallow water stream down a steep slope, *Journal of Fluid Mechanics*, *595*, 83-114, doi:10.1017/S0022112007008774

Aranson, I.S., Tsimring, L.S., Malloggi, F. and Clément, E. (2008). Nonlocal rheological properties of granular flows near a jamming limit. Physical Review E, 78(031303): 14.

Arulanandan, K., and Perry, E. B. (1983). Erosion in relation to filter design criteria in Earth dams, *Journal of Geotechnical Engineering*, *109*, 682-698.

Behringer, R.P., Dapeng, B., Charkraborty, B., Henkes, S. and Hartley, R.R. (2008). Why do granular materials stiffen with shear rate? Test of novel stress-based statistics. Physical Rev. Letters, 101(268301).

Berger, C., McArdell, B.W. and Schlunegger, F. (2011). Direct measurement of channel erosion by debris flows, Illgraben, Switzerland. Journal of Geophysical Research, 116(F01002): 18.

Bernard, B., Van Wyk de Vries, B., Barba, D., Leyrit, H., Robin, C., Alcaraz, S., and Samaniego, P. (2008). The Chimborazo sector collapse and debris avalanche: Deposit characteristics as evidence of emplacement mechanisms. Journal of Volcanology and Geothermal Research, 176: 36-43

Boyalakuntla, D.S. (2003). Simulation of granular and gas-solid flows using discrete element method. PhD Thesis, Carnegie Mellon University: 210.

Brewster, R., Silbert, L., Grest, G., and Levine, A. (2008). Relationship between interparticle contact lifetimes and rheology in gravity-driven granular flows. Physical Review E, 77: 12.

Branney, M., and Kokelaar, B. (2002). Pyroclastic density currents and the sedimentation of ignimbrites. Memoirs of the Geological Society of London, 27: 8.

Bursik, M., Patra, A., Pitman, E.B., Nichita, C., Macias, J.L., Saucedo, R. and Girina, O. (2005). Advances in studies of dense volcanic granular flows. Reports on Progress in Physics, 68: 31.

Calder, E.S., Sparks, R.S.J. and Gradeweg, M.C. (2000). Erosion, transport and segregation of pumic and lithic clasts in pyroclastic flows inferred from ignimbrite at Lascar Volcano, Chile. Journal of Volcanology and Geothermal Research, 104(1-4): 26.

Campbell, C.S. (2006). Granular material flows - An overview. Powder Tech., 162: 22.

Campbell, C. S. (2003), A problem related to the stability of force chains, *Granular Matter*, *5*, 129-134, doi:10.1007/s10035-003-0138-6

Cole, D.M. and Peters, J.F. (2008). Grain-scale mechanics of geologic materials and lunar simulants under normal loading. Granular Matter, 10: 171.

Coste, C. and Giles, B. (1999). On the validity of Hertz contact law for granular material acoustics. European Physical Journal B, 7(1): 11.

Crosta, G.B., Imposimato, S. and Roddeman, D. (2009). Numerical modeling of entrainment/deposition in rock and debris-avalanches. Engineering Geology, 109: 11.

Cundall, P.A. and Strack, O.D.L. (19790. A discrete numerical model for granular assemblies. Géotechnique, 29(1): 19.

Daniels, K. E. and Hayman, N. W. (2008), Force chains in seismogenic faults visualized with photoelastic granular shear experiments, *Journal of Geophysical Research, 113(B11411*), doi:10.1029/2008JB005781.

Davies, T., McSaveney, M. and Kelfoun, K. (2010). Runout of the Socompa volcanic debris avalanche, Chile: a mechanical explanation for low basal shear resistance. Bulletin of Volcanology, 72(8): 12.

Davies, T.R. and McSaveney, M.J. (2009). The role of rock fragmentation in the motion of large landslides. Engineering Geology, 109(13): 67.

De Blasio, F.V. (2011). Dynamical stress in force chains of granular media traveling on a bumpy terrain and the fragmentation of rock avalanches. Acta Mech, 221: 8.

Denlinger, R.P. and Iverson, R.M. (2004). Granular avalanches across irregular three-dimensional terrain, 1. Theory and computation. Journal of Geophysical Research, Earth Surface, 109(F1): 14.

Dufek, J. and Bergantz, G.W. (2007). Dynamics and deposits generated by the Kos Plateau Tuff eruption: Controls of basal particle loss on pyroclastic flow transport. Geochemistry, Geophysics, Geosystems, 8: Q12007.

Dufek, J. and Manga, M. (2008). In situ production of ash in pyroclastic flows. Journal of Geophysical Research, 113(B9): B09207.

Dufek, J., Wexler, J. and Manga, M. (2009). Transport capacity of pyroclastic density currents: Experiments and models of substrate-flow interaction. Journal of Geophysical Research - Solid Earth, 114(DOI: 10.1029/2008JB006216): B11203.

Dutilleul, P., Stockwell, J. D., Frigon, D., and Legendre, P. (2000), The Mantel test versus Pearson's correlation analysis: Assessment of the differences for biological and environmental studies, *Journal of Agricultural, Biological, and Environmental Statistics, 5(2)*, 131-150, doi:10.2307/1400528

Eringen, A. C. (2004), A mixture theory for geophysical fluids, *Nonlinear Processes in Geophysics, 11*, 75-82.

Estep, J. and Dufek, J. (2013). Discrete element simulations of bed force anomalies due to force chains in dense granular flows. Journal of Volcanology and Geothermal Research, 254: 108-117.

Estep, J. and Dufek, J. (2012). Substrate effects from force chain dynamics in dense granular flows. Journal of Geophysical Research, Earth Surface, 117(F01028): 12.

Frey, P., and Church, M. (2011), Bedload: a granular phenomenon, *Earth Surface Processes and Landforms, 36*, 58-69, doi:10.1002/esp.2103

Furbish, D.J., Schmeeckle, M.W. and Roering, J.J. (2008). Thermal and force-chain effects in an experimental, sloping granular shear flow. Earth Surface Process Landforms, 33: 10.

Garcia M., and Parker G. (1991), Entrainment of bed sediment into suspension, *Journal of Hydraulic Engineering, 117*, 414-435.

Garg, R., Galvin, J., Li, T. and Pannala, S. (2010). Documentation of open-source MFIX-DEM software for gas-solids flows.

Geng, J., Reydellet, G., Clément, E. and Behringer, R.P. (2003). Green's function measurements of force transmission in 2D granular materials. Physica D, 182: 30.

Gray, J., Wieland, M. and Hutter, K. (1999). Gravity-driven free surface flow of granular avalanches over complex basal topography. Proceedings of the Royal Society of London Series A - Mathematical Physical and Engineering Sciences, 455(1985): 5.

Grunewald, U., Sparks, R.S., Kearns, S., Komorowski, J.C. (2000). Friction marks on blocks from pyroclastic flows at the Soufriere Hills volcano, Montserrat: Implications for flow mechanisms. Geology, 28: 827-830

Huppert, H. and Dade, W.B. (1998). Natural disasters: Explosive volcanic eruptions and gigantic landslides. Theoretical and Computational Fluid Dynamics, 10: 13.

Iverson, R.M., Reid, M.E., Logan, M., LaHusen, R.G., Godt, J.W. and Griswold, J.P. (2011). Positive feedback and momentum growth during debris-flow entrainment of wet bed sediment. Nature Geoscience, 4: 6.

Iverson, R. (1997), The physics of debris flows, *Reviews of Geophysics, 35*, 245-296.

Jaeger, H. M., Nagel, S. R., and Behringer, R. P. (1996), Granular solids, liquids, and gases, *Reviews of Modern Physics 68*, 1259-1273.

Ji, S. and Shen, H.H. (2006). Effect of contact force models on granular flow dynamics. Journal of Engineering Mechanics, 132(11): 8.

Kelfoun, K. (2011). Suitability of simple rheological laws for the numerical simulation of dense pyroclastic flows and long-runout volcanic avalanches. Journal of Geophysical Research, 116(B08209): 14.

LaBerge, R. D., Giordano, G., Cas, R., and Allieres, L. (2006), Syn-depositional substrate deformation produced by the shear force of a pyroclastic density current: An example from the Pleistocene ignimbrite at Monte Cimino,

northern Lazio, Italy, *Journal of Volcanology and Geothermal Research, 158,* 307-320, doi:10.1016/j.jvolgeores.2006.07.003

Majmudar, T. S., Sperl, M., Luding, S., and Behringer, R. P. (2007), Jamming transition in granular systems, *Physical Review Letters, 98(058001-1-058001-4),* doi:10.1103/PhysRevLett.98.058001

Majmudar, T.S. and Behringer, R.P. (2005). Contact force measurements and stress-induced anisotropy in granular materials. Nature, 435: 4.

Malone, K.F. and Xu, B.H. (2008). Determination of contact parameters for discrete element method simulations of granular systems. Particuology, 6: 8.

Mangeney, A., Roche, O., Hungr, O., Mangold, N., Faccanoni, G. and Lucas, A. (2010). Erosion and mobility in granular collapse over sloping beds. Journal of Geophysical Research, 115: F03040.

Mangeney, A., Tsimring, L.S., Volfson, D., Aranson, I.S. and Bouchet, F. (2007). Avalanche mobility induced by the presence of an erodible bed and associated entrainment. Geophysical Research Letters, 34(L22401).

Manville, V., Nemeth, K. and Kano, K. (2009). Source to sink: A review of three decades of progress in the understanding of volcaniclastic processes, deposits, and haszards. Sedimentary Geology, 220: 26.

Massey, C., Hodgson, I. and Petley, D. (2006). A rockfall simulation study for housing development in Gebraltar. The Geological Society of London, IAEG2006 Paper number 377: 9.

McDougall, S. and Hungr, O. (2005). Dynamic modeling of entrainment in rapid landslides. Canadian Geotechnical Journal, 42: 12.

Milburn, R.J., Naylor, M.A., Smith, A.J., Leaper, M.C., Good, K., Swift, M.R. and King, P.J. (2005). Faraday tilting of water-immersed granular beds. Physical Review E, 71(1).

Moreno-Atanasio, R., Xu, B.H. and Ghadiri, M. (2007). Computer simulation of the effect of contact stiffness and adhesion on the fluidization behaviour of powders. Chemical Engineering Science, 62: 11.

Muthuswamy, M. and Antionette, T. (2006). How do interparticle contact friction, packing density, and degree of polydispersity affect force propagation in

particulate assemblies? Journal of Statistical Mechanics: Theory and Experiment (P09003).

Ongaro, T., Clarke, A., Voight, B., Neri, A., and Widiwijayanti, C. (2012). Multiphase flow dynamics of pyroclastic density currents during the May 18, 1980 lateral blast of Mount St. Helens. Journal of Geophysical Research, 117 (B06208).

Pirulli, M. (2010). Morphology and substrate control on the dynamics of flowlike landslides. Journal of Geotechnical and Geoenvironmental Engineering, 136(2): 13.

Ponomareva, V., Melekestsev, I., Dirksen, O. (2006). Sector collapses and large landslides on Late Pleistocene-Holocene volcanoes in Kamchatka, Russia. Journal of Volcanology and Geothermal Research, 158: 117-138.

Pudasaini, S.P., Wang, Y. and Hutter, K. (2005). Modeling debris flows down general channels. Natural Hazards and Earth System Sciences, 5: 21.

Rattanadit, K., Florin, B., Promratana, K. and Turner, J. (2009). Force chains and resonant behavior in bending of a granular layer on an elastic support. Mechanics of Materials, 41: 16.

Reddy, K. and Kumaran, V. (2010). Dense granular flow down an inclined plane: A comparison between the hard particle model and soft particle simulations. Physics of Fluids, 22(113302).

Roche, O. (2012). Depositional processes and gas pore pressure in pyroclastic flows: an experimental perspective. Bulletin of Volcanology, 74(8): 1807-1820.

Rycroft, C.H., Kamrin, K. and Bazant, M.Z. (2009). Assessing continuum postulates in simulations of granular flow. Journal of the Mechanics and Physics of Solids, 57(5): 12.

Santamarina, C., Klein, K., and Fam, M. (2001) Soils and Waves: John Wiley and Sons, Ltd. West Sussex, England. ISBN 0-471-49058-X

Sarmiento, O. S., and Falcon, M. (2006), Critical bed shear stress for unisize sediment, *Journal of Hydraulic Engineering, (132)*, 172-179, doi:10.1061/(ASCE)0733-9429(2006)132:2(172)

Sarocchi, D., Sulpizio, R., Macias, J.L. and Saucedo, R. (2011). The 17 July 1999 block-and-ash flow (BAF) at Colima Volcano: New Insights on volcanic

granular flows from textural analysis. Journal of Volcanology and Geothermal Research, 204(1-4): 17.

Silbert, L.E., Landry, J.W. and Grest, G.S. (2002). Granular flow down a rough inclined plane: Transition between thin and thick piles. Physics of Fluids, 15(1): 10.

Schwaiger, H. F., and Higman, B. (2007), Lagrangian hydrocode simulations of the 1958 Lituya Bay tsunami-genic rockslide, *Geochemistry, Geophysics, Geosystems, 8(G07006),* doi:10.1029/2007GC001584.

Schuerch, P., Densmore, A. L., Rosser, N. J., and McArdell, B. W. (2011), Dynamic controls on erosion and deposition on debris-flow fans, *Geology, 39*, 827-830, doi:10.1130/G32103.1

Sun, Q., Jin, F. and Liu, J. (2010). Understanding force chains in dense granular materials. International Journal of Modern Physics B, 24(29): 17.

Thompson, N.D., Bennett, M.R. and Petford, N. (2010). Development of characteristic volcanic debris avalanche deposit structures: new insight from distinct element simulations. Journal of Volcanology and Geothermal Research, 192(3-4): 10.

Ting, J.M., Corkum, B.T., Kauffman, C.R. and Greco, C. (1989). Discrete numerical model for soil mechanics. Journal of Geotechnical Engineering, 115(3): 20.

Trauth, M. H. (2007), *Matlab Recipes for Earth Sciences*, Springer-Verlag. Second Edition.

Tsuji, Y., Kawaguchi, T. and Tanaka, T. (1993). Discrete particle simulation of two-dimensional fluidized bed. Powder Tech., 77(1): 9.

Vishay Precision Group (2010), Calibration of low-modulus PhotoStress coatings: Application note IB-238-1. Micro-Measurements, *www.micro-measurments.com. 4-12-2011. Document No.: 11238*, 1-2.

Vreugdenhil, C. B. (1994), *Numerical Methods for Shallow Water Flow,* Kluwer Acad., Norwell, Mass.

Yuu, S., Abe, T., Saitoh, T. and Umekage, T. (1995). Three-dimensional numerical simulation of the motion of particles discharging from a rectangular hopper using distinct element method and comparison with

experimental data (effects of time steps and material properties). Advanced Powder Technology, 6(4): 11.

Zanuttigh, B. and Lamberti, A. (2007). Instability and surge development in debris flows. Reviews of Geophysics, 45(RG3006): 45.

VITA

JOSEPH (JOE) J. ESTEP

Joe was born in Newnan, Georgia, which is located about 40 miles south of Atlanta. He has been a resident of Georgia for his entire life, and has previously earned his B.S. and M.S. in Earth and Atmospheric Sciences from Georgia Tech in 2009 and 2011, respectively. Joe is the youngest of four children; but is, hands down, the coolest and best looking out of the bunch.

When he realized his aspirations of becoming a professional athlete or racecar driver didn't show promise, Joe opted to focus on developing his most powerful muscle – his brain. Choosing the earth science field was a likely consequence of an aptitude for math and science being combined with awe and curiosity about the natural world. His participation in the Physical Volcanology research group at Georgia Tech, however, was a delightfully surprising result of good timing, a bit of luck, but mostly probably was due to being the most awesome student ever. Joe doesn't tend to share this information, but he has superpowers. He can fly; shoot lasers from his eyes, and possesses The Force.

Joe is a sports guy, and is happy to compete at just about anything. He was a stand out baseball player until experiencing a rash of injuries in high school that derailed plans to compete in college. He now enjoys playing golf, tailgating sports, intramurals, and just about anything that can get the competitive juices flowing. Joe is a fan of all Atlanta professional sports teams and particularly enjoys going to Braves games with family, friends, or new acquaintances. Upon graduation Joe has plans to move to Houston, Texas where he has accepted a position with Chevron Energy Technology Company.